Z boson decays $Z \to l_i^{\pm} l_j^{\mp}$ and Higgs boson decays $h \to l_i^{\pm} l_j^{\mp}$ with lepton flavor violation in a $U(1)$ extension of the MSSM

Yi-Tong Wang,[1,2,*] Shu-Min Zhao,[1,2,†] Tong-Tong Wang,[1,2] Xi Wang,[1,2] Xin-Xin Long,[1,2] Jiao Ma,[1,2] and Tai-Fu Feng[1,2,3]

[1]Department of Physics, Hebei University, Baoding 071002, China
[2]Key Laboratory of High-precision Computation and Application of Quantum Field Theory of Hebei Province, Baoding 071002, China
[3]Department of Physics, Chongqing University, Chongqing 401331, China

(Received 6 July 2022; accepted 9 September 2022; published 29 September 2022)

The $U(1)$ extension of the supersymmetric standard model is the extension of the minimal supersymmetric standard model, and its local gauge group is $SU(3)_C \times SU(2)_L \times U(1)_Y \times U(1)_X$. We study lepton flavor violating (LFV) decays $Z \to l_i^{\pm} l_j^{\mp}$ ($Z \to e\mu$, $Z \to e\tau$, and $Z \to \mu\tau$) and $h \to l_i^{\pm} l_j^{\mp}$ ($h \to e\mu$, $h \to e\tau$, and $h \to \mu\tau$) in this model. In the numerical results, the branching ratios of $Z \to l_i^{\pm} l_j^{\mp}$ are from 10^{-9} to 10^{-13}, and the branching ratios of $h \to l_i^{\pm} l_j^{\mp}$ are from 10^{-3} to 10^{-9}, which can approach the present experimental upper bounds. Based on the latest experimental data, we analyze the influence of different sensitive parameters on the branching ratio and make reasonable predictions for future experiments. The main sensitive parameters and LFV sources are the nondiagonal elements corresponding to the initial and final generations of leptons, which can be seen from the numerical analysis.

DOI: 10.1103/PhysRevD.106.055044

I. INTRODUCTION

Neutrinos have tiny masses and mix with each other, as proved by the neutrino oscillation experiment [1,2]. This indicates that the lepton flavor symmetry is not conservative in the neutrino region. The Large Hadron Collider (LHC) can detect about 125 GeV new particles [3,4], whose properties are close to those of the Higgs boson, which is very successful for the standard model (SM). The LFV decays are forbidden in the SM. If LFV decays of charged leptons are detected, we have direct evidence of new physics (NP). The LFV decays of Higgs bosons and Z bosons are of interest, opening a window for detecting NP beyond the SM.

In Table I, we summarize the current limitations and future prospects of the three modes of the Z boson ($Z \to e\mu$, $Z \to e\tau$, and $Z \to \mu\tau$) [5–10]. For the Large Electron-Positron Collider (LEP), the most stringent upper limit is to use a data sample of 5×10^6 Z bosons produced in e^+e^- collisions [5]. The LHC has already produced many more Z bosons in pp collisions. The upper limit on the branching ratio by the ATLAS experiment corresponds to 7.8×10^8 Z bosons being produced [5], significantly more restrictive than that from the LEP experiments. For the future sensitivity of CEPC and FCC-ee circular e^+e^- colliders assuming 3×10^{12} Z decays [6], they are about 6 orders of magnitude more than LEP experiments. Moreover, at least for the $Z \to e\tau$ and $Z \to \mu\tau$, CEPC/FCC-ee could improve the present LHC (future HL-LHC) bounds by up to 4 (3) orders of magnitude.

For $h \to l_i^{\pm} l_j^{\mp}$ ($h \to e\mu$, $h \to e\tau$, and $h \to \mu\tau$), due to low energy constraints, $h \to e\mu$ is more suppressed than $h \to e\tau$ and $h \to \mu\tau$. Moreover, since the LHC searches for $h \to e\tau$ and $h \to \mu\tau$, the discovery of LFV at the LHC or future leptonic colliders is still an open possibility. After the discovery of the Higgs boson, some future experiments have been proposed to study the properties of the Higgs boson, including two circular lepton colliders (CEPC and FCC-ee) and a linear lepton collider (ILC). In Table II, we summarize the current limitations and future sensitivity on LFV Higgs decays [11–14].

Combining the experimental data provided by ATLAS and CMS, the upper limits on the LFV branching ratios of $Z \to e\mu$, $Z \to e\tau$, $Z \to \mu\tau$ and $h \to e\mu$, $h \to e\tau$, $h \to \mu\tau$ at 95% confidence level (C.L.) are shown in Table III [15–19]. The LFV decays can easily occur in NP models beyond the SM, for instance, in supersymmetric models and others [20,21]. Due to the running of the LHC, the LFV decays have recently been discussed within various theoretical frameworks [22–27].

*wyt_991222@163.com
†zhaosm@hbu.edu.cn

TABLE I. Current upper limits on LFV Z decays from LEP and LHC experiments and future sensitivity from CEPC/FCC-ee.

Decay modes	LEP (95% C.L.)	LHC (95% C.L.)	CEPC/FCC-ee
$Z \to e\mu$	1.7×10^{-6} [5]	7.5×10^{-7} [5]	$10^{-8} - 10^{-10}$ [10]
$Z \to e\tau$	9.8×10^{-6} [6,7]	5.0×10^{-6} [9]	10^{-9} [10]
$Z \to \mu\tau$	1.2×10^{-5} [6,8]	6.5×10^{-6} [9]	10^{-9} [10]

The $U(1)_X$ of the supersymmetric standard model (SSM) is the extension of the minimal supersymmetric standard model (MSSM), and its local gauge group is $SU(3)_C \times SU(2)_L \times U(1)_Y \times U(1)_X$ [28–30]. To obtain this model, three new singlet Higgs superfields and right-handed neutrinos are added to the MSSM. In this work, we analyze the LFV decays $Z \to l_i^{\pm} l_j^{\mp}$ ($Z \to e\mu$, $Z \to e\tau$, and $Z \to \mu\tau$) and $h \to l_i^{\pm} l_j^{\mp}$ ($h \to e\mu$, $h \to e\tau$, and $h \to \mu\tau$) within the $U(1)_X$SSM model. Compared with the MSSM, the neutrino masses in the $U(1)_X$SSM are not zero. These new sources enlarge the LFV processes via loop contributions. Therefore, the expected experimental results for the LFV processes may be obtained in the near future.

In our previous work, we studied the LFV decays $l_j \to l_i\gamma$ in the $U(1)_X$SSM [31]. The numerical results showed that the present experimental limits for the branching ratio of $l_j \to l_i\gamma$ constrain the parameter space of the $U(1)_X$SSM most strictly. In this work, considering the constraint of the present experimental limits on the branching ratio of $l_j \to l_i\gamma$, we show the influence of slepton flavor mixing parameters on the branching ratios of $Z \to l_i^{\pm} l_j^{\mp}$, $h \to l_i^{\pm} l_j^{\mp}$, and $l_j \to l_i\gamma$ in the $U(1)_X$SSM.

Our paper is organized as follows. In Sec. II, we briefly introduce the main content of the $U(1)_X$SSM, including its superpotential, the general soft SUSY-breaking terms, mass matrices, and couplings. Sections III and IV are devoted to the decays $Z \to l_i^{\pm} l_j^{\mp}$ and $h \to l_i^{\pm} l_j^{\mp}$ with lepton flavor violation in the $U(1)_X$SSM. In Sec. V, we give the corresponding parameters and numerical analysis. A discussion and conclusions are given in Sec. VI. The Appendix introduces some specific forms of coupling coefficients that we need for this work.

II. MAIN CONTENT OF $U(1)_X$SSM

The $U(1)_X$SSM is the $U(1)$ extension of the MSSM, and the local gauge group is $SU(3)_C \otimes SU(2)_L \otimes U(1)_Y \otimes U(1)_X$ [31–34]. In order to obtain the $U(1)_X$SSM, the MSSM has added new superfields, including right-handed neutrinos $\hat{\nu}_i$ and three Higgs singlets, $\hat{\eta}, \hat{\bar{\eta}}, \hat{S}$. Through the seesaw mechanism, light neutrinos obtain tiny masses at the tree level. The neutral CP-even parts of $H_u, H_d, \eta, \bar{\eta}$, and S mix together, forming a 5×5 mass squared matrix. The loop corrections to the lightest CP-even Higgs are needed in order to get the Higgs mass of 125.1 GeV [35,36]. The sneutrinos are disparted into CP-even sneutrinos and CP-odd sneutrinos, and their mass squared matrices are both extended to 6×6.

The superpotential in the $U(1)_X$SSM is expressed as

$$\begin{aligned} W = {} & l_W \hat{S} + \mu \hat{H}_u \hat{H}_d + M_S \hat{S}\,\hat{S} - Y_d \hat{d}\,\hat{q}\,\hat{H}_d - Y_e \hat{e}\,\hat{l}\,\hat{H}_d \\ & + \lambda_H \hat{S} \hat{H}_u \hat{H}_d + \lambda_C \hat{S}\,\hat{\eta}\,\hat{\bar{\eta}} + \frac{\kappa}{3} \hat{S}\,\hat{S}\,\hat{S} + Y_u \hat{u}\,\hat{q}\,\hat{H}_u \\ & + Y_X \hat{\nu}\,\hat{\bar{\eta}}\,\hat{\nu} + Y_\nu \hat{\nu}\,\hat{l}\,\hat{H}_u. \end{aligned} \tag{1}$$

The specific explicit expressions of two Higgs doublets are as follows:

$$\begin{aligned} H_u &= \begin{pmatrix} H_u^+ \\ \frac{1}{\sqrt{2}}(v_u + H_u^0 + iP_u^0) \end{pmatrix}, \\ H_d &= \begin{pmatrix} \frac{1}{\sqrt{2}}(v_d + H_d^0 + iP_d^0) \\ H_d^- \end{pmatrix}. \end{aligned} \tag{2}$$

The three Higgs singlets are represented by

$$\begin{aligned} \eta &= \frac{1}{\sqrt{2}}(v_\eta + \phi_\eta^0 + iP_\eta^0), \qquad \bar{\eta} = \frac{1}{\sqrt{2}}(v_{\bar{\eta}} + \phi_{\bar{\eta}}^0 + iP_{\bar{\eta}}^0), \\ S &= \frac{1}{\sqrt{2}}(v_S + \phi_S^0 + iP_S^0). \end{aligned} \tag{3}$$

Here, v_u, v_d, v_η, $v_{\bar{\eta}}$, and v_S are the corresponding vacuum expectation values (VEVs) of the Higgs superfields

TABLE II. Current upper limits and future sensitivity on LFV Higgs decays.

Decay modes	LHC (95% C.L.)	CEPC/FCC-ee	ILC
$h \to e\mu$	6.2×10^{-5} [11–13]	1.2×10^{-5} [14]	2.1×10^{-5} [14]
$h \to e\tau$	4.7×10^{-3} [11–13]	1.6×10^{-4} [14]	2.4×10^{-4} [14]
$h \to \mu\tau$	2.5×10^{-3} [11–13]	1.4×10^{-4} [14]	2.3×10^{-4} [14]

TABLE III. Upper limits on the LFV branching ratios of $Z \to l_i^{\pm} l_j^{\mp}$ and $h \to l_i^{\pm} l_j^{\mp}$.

Decay modes	Z boson	Higgs boson
$e\mu$	7.5×10^{-7}	6.2×10^{-5}
$e\tau$	9.8×10^{-6}	4.7×10^{-3}
$\mu\tau$	1.2×10^{-5}	2.5×10^{-3}

TABLE IV. Superfields in the $U(1)_X$SSM.

Superfields	$\hat{q}_i$	$\hat{u}_i^c$	$\hat{d}_i^c$	$\hat{l}_i$	$\hat{e}_i^c$	$\hat{\nu}_i$	$\hat{H}_u$	$\hat{H}_d$	$\hat{\eta}$	$\hat{\bar{\eta}}$	$\hat{S}$
$SU(3)_C$	3	$\bar{3}$	$\bar{3}$	1	1	1	1	1	1	1	1
$SU(2)_L$	2	1	1	2	1	1	2	2	1	1	1
$U(1)_Y$	1/6	−2/3	1/3	−1/2	1	0	1/2	−1/2	0	0	0
$U(1)_X$	0	−1/2	1/2	0	1/2	−1/2	1/2	−1/2	−1	1	0

H_u, H_d, η, $\bar{\eta}$, and S. Two angles are defined as $\tan\beta = v_u/v_d$ and $\tan\beta_\eta = v_{\bar{\eta}}/v_\eta$. The definitions of $\tilde{\nu}_L$ and $\tilde{\nu}_R$ are

$$\tilde{\nu}_L = \frac{1}{\sqrt{2}}\phi_l + \frac{i}{\sqrt{2}}\sigma_l, \qquad \tilde{\nu}_R = \frac{1}{\sqrt{2}}\phi_R + \frac{i}{\sqrt{2}}\sigma_R. \tag{4}$$

The soft SUSY-breaking terms of the $U(1)_X$SSM are

$$\begin{aligned}\mathcal{L}_{\text{soft}} = {} & \mathcal{L}_{\text{soft}}^{\text{MSSM}} - B_S S^2 - L_S S - \frac{T_\kappa}{3} S^3 - T_{\lambda_C} S\eta\bar{\eta} \\ & + \epsilon_{ij} T_{\lambda_H} S H_d^i H_u^j - T_X^{IJ} \bar{\eta} \tilde{\nu}_R^{*I} \tilde{\nu}_R^{*J} + \epsilon_{ij} T_\nu^{IJ} H_u^i \tilde{\nu}_R^{I*} \tilde{l}_j^J \\ & - m_\eta^2 |\eta|^2 - m_{\bar{\eta}}^2 |\bar{\eta}|^2 - m_S^2 S^2 - (m_{\tilde{\nu}_R}^2)^{IJ} \tilde{\nu}_R^{I*} \tilde{\nu}_R^J \\ & - \frac{1}{2}(M_X \lambda_{\tilde{X}}^2 + 2 M_{BB'} \lambda_{\tilde{B}} \lambda_{\tilde{X}}) + \text{H.c.}\end{aligned} \tag{5}$$

Table IV shows the particle content and charge distribution of the $U(1)_X$SSM. We have shown that the $U(1)_X$SSM is anomaly free in previous work [34]. The two Abelian groups $U(1)_Y$ and $U(1)_X$ in the $U(1)_X$SSM cause a new effect: the gauge kinetic mixing. This effect can be induced by renormalization group equations (RGEs).

The general form of the covariant derivative of the $U(1)_X$SSM can be found in Refs. [37–40]. In the $U(1)_X$SSM, the gauge bosons A_μ^X, A_μ^Y, and V_μ^3 mix together at the tree level. The mass matrix in the basis $(A_\mu^Y, V_\mu^3, A_\mu^X)$ can be found in Ref. [34]. We use two mixing angles θ_W and θ'_W to obtain mass eigenvalues of the matrix. Here, θ_W is the Weinberg angle, and θ'_W is the new mixing angle. The new mixing angle is defined as

$$\sin^2\theta'_W = \frac{1}{2} - \frac{[(g_{YX}+g_X)^2 - g_1^2 - g_2^2]v^2 + 4g_X^2\xi^2}{2\sqrt{[(g_{YX}+g_X)^2 + g_1^2 + g_2^2]^2 v^4 + 8g_X^2[(g_{YX}+g_X)^2 - g_1^2 - g_2^2]v^2\xi^2 + 16 g_X^4 \xi^4}}. \tag{6}$$

Here, $v^2 = v_u^2 + v_d^2$ and $\xi^2 = v_\eta^2 + v_{\bar{\eta}}^2$.

The new mixing angle appears in the couplings involving Z and Z'. The exact eigenvalues are calculated as

$$\begin{aligned} m_\gamma^2 &= 0, \\ m_{Z,Z'}^2 &= \frac{1}{8}([g_1^2 + g_2^2 + (g_{YX}+g_X)^2]v^2 + 4g_X^2\xi^2 \\ &\quad \mp \sqrt{[g_1^2 + g_2^2 + (g_{YX}+g_X)^2]^2 v^4 + 8[(g_{YX}+g_X)^2 - g_1^2 - g_2^2]g_X^2 v^2\xi^2 + 16 g_X^4 \xi^4}). \end{aligned} \tag{7}$$

The mass squared matrix for CP-even Higgs $(\phi_d, \phi_u, \phi_\eta, \phi_{\bar{\eta}}, \phi_s)$ reads

$$M_h^2 = \begin{pmatrix} m_{\phi_d\phi_d} & m_{\phi_u\phi_d} & m_{\phi_\eta\phi_d} & m_{\phi_{\bar{\eta}}\phi_d} & m_{\phi_s\phi_d} \\ m_{\phi_d\phi_u} & m_{\phi_u\phi_u} & m_{\phi_\eta\phi_u} & m_{\phi_{\bar{\eta}}\phi_u} & m_{\phi_s\phi_u} \\ m_{\phi_d\phi_\eta} & m_{\phi_u\phi_\eta} & m_{\phi_\eta\phi_\eta} & m_{\phi_{\bar{\eta}}\phi_\eta} & m_{\phi_s\phi_\eta} \\ m_{\phi_d\phi_{\bar{\eta}}} & m_{\phi_u\phi_{\bar{\eta}}} & m_{\phi_\eta\phi_{\bar{\eta}}} & m_{\phi_{\bar{\eta}}\phi_{\bar{\eta}}} & m_{\phi_s\phi_{\bar{\eta}}} \\ m_{\phi_d\phi_s} & m_{\phi_u\phi_s} & m_{\phi_\eta\phi_s} & m_{\phi_{\bar{\eta}}\phi_s} & m_{\phi_s\phi_s} \end{pmatrix}, \tag{8}$$

$$\begin{aligned} m_{\phi_d\phi_d} = {} & m_{H_d}^2 + |\mu|^2 + \frac{1}{8}([g_1^2 + (g_X + g_{YX})^2 \\ & + g_2^2](3v_d^2 - v_u^2) + 2(g_{YX}g_X + g_X^2)(v_\eta^2 - v_{\bar{\eta}}^2)) \\ & + \sqrt{2} v_S \mu \lambda_H + \frac{1}{2}(v_u^2 + v_S^2)|\lambda_H|^2, \end{aligned} \tag{9}$$

$$\begin{aligned} m_{\phi_d\phi_u} = {} & -\frac{1}{4}(g_2^2 + (g_{YX}+g_X)^2 + g_1^2) v_d v_u + |\lambda_H|^2 v_d v_u \\ & - \lambda_H l_W - \frac{1}{2}\lambda_H (v_\eta v_{\bar{\eta}} \lambda_C + v_S^2 \kappa) \\ & - B_\mu - \sqrt{2} v_S \left(\frac{1}{2} T_{\lambda_H} + M_S \lambda_H\right), \end{aligned} \tag{10}$$

$$m_{\phi_u\phi_u} = m_{H_u}^2 + |\mu|^2 + \frac{1}{8}([g_1^2 + (g_X + g_{YX})^2 + g_2^2](3v_u^2 - v_d^2) + 2(g_{YX}g_X + g_X^2)(v_{\bar{\eta}}^2 - v_\eta^2)) + \sqrt{2}v_S\mu\lambda_H + \frac{1}{2}(v_d^2 + v_S^2)|\lambda_H|^2, \quad (11)$$

$$m_{\phi_d\phi_\eta} = \frac{1}{2}g_X(g_{YX} + g_X)v_d v_\eta - \frac{1}{2}v_u v_{\bar{\eta}}\lambda_H\lambda_C, \quad (12)$$

$$m_{\phi_u\phi_\eta} = -\frac{1}{2}g_X(g_{YX} + g_X)v_u v_\eta - \frac{1}{2}v_d v_{\bar{\eta}}\lambda_H\lambda_C, \quad (13)$$

$$m_{\phi_\eta\phi_\eta} = m_\eta^2 + \frac{1}{4}((g_{YX}g_X + g_X^2)(v_d^2 - v_u^2) + 2g_X^2(3v_\eta^2 - v_{\bar{\eta}}^2)) + \frac{|\lambda_C|^2}{2}(v_{\bar{\eta}}^2 + v_S^2), \quad (14)$$

$$m_{\phi_d\phi_{\bar{\eta}}} = -\frac{1}{2}g_X(g_{YX} + g_X)v_d v_{\bar{\eta}} - \frac{1}{2}v_u v_\eta\lambda_H\lambda_C, \quad (15)$$

$$m_{\phi_u\phi_{\bar{\eta}}} = \frac{1}{2}g_X(g_{YX} + g_X)v_u v_{\bar{\eta}} - \frac{1}{2}v_d v_\eta\lambda_H\lambda_C, \quad (16)$$

$$m_{\phi_\eta\phi_{\bar{\eta}}} = -g_X^2 v_\eta v_{\bar{\eta}} + \frac{1}{2}(2l_W - \lambda_H v_d v_u)\lambda_C + |\lambda_C|^2 v_\eta v_{\bar{\eta}} + \frac{1}{\sqrt{2}}v_S(2M_S\lambda_C + T_{\lambda_C}) + \frac{1}{2}v_S^2\lambda_C\kappa, \quad (17)$$

$$m_{\phi_{\bar{\eta}}\phi_{\bar{\eta}}} = m_{\bar{\eta}}^2 + \frac{1}{4}((g_{YX}g_X + g_X^2)(v_u^2 - v_d^2) + 2g_X^2(3v_{\bar{\eta}}^2 - v_\eta^2)) + \frac{|\lambda_C|^2}{2}(v_\eta^2 + v_S^2), \quad (18)$$

$$m_{\phi_d\phi_s} = (\lambda_H v_d v_S + \sqrt{2}v_d\mu - v_u(\kappa v_S + \sqrt{2}M_S))\lambda_H - \frac{1}{\sqrt{2}}v_u T_{\lambda_H}, \quad (19)$$

$$m_{\phi_u\phi_s} = (\lambda_H v_u v_S + \sqrt{2}v_u\mu - v_d(\kappa v_S + \sqrt{2}M_S))\lambda_H - \frac{1}{\sqrt{2}}v_d T_{\lambda_H}, \quad (20)$$

$$m_{\phi_\eta\phi_s} = (\lambda_C v_\eta v_S + v_{\bar{\eta}}(\kappa v_S + \sqrt{2}M_S))\lambda_C + \frac{1}{\sqrt{2}}v_{\bar{\eta}}T_{\lambda_C}, \quad (21)$$

$$m_{\phi_{\bar{\eta}}\phi_s} = (\lambda_C v_{\bar{\eta}} v_S + v_\eta(\kappa v_S + \sqrt{2}M_S))\lambda_C + \frac{1}{\sqrt{2}}v_\eta T_{\lambda_C}, \quad (22)$$

$$m_{\phi_s\phi_s} = m_S^2 + (2l_W + 3v_S(\kappa v_S + 2\sqrt{2}M_S) + \lambda_C v_\eta v_{\bar{\eta}} - \lambda_H v_d v_u)\kappa + \frac{1}{2}|\lambda_C|^2\xi^2 + \frac{1}{2}|\lambda_H|^2 v^2 + 2B_S + 4|M_S|^2 + \sqrt{2}v_S T_\kappa. \quad (23)$$

This matrix is diagonalized by Z^H:

$$Z^H m_h^2 Z^{H,\dagger} = m_{2,h}^{\mathrm{dia}}, \quad (24)$$

with

$$\phi_d = \sum_j Z_{j1}^H h_j, \qquad \phi_u = \sum_j Z_{j2}^H h_j, \qquad \phi_\eta = \sum_j Z_{j3}^H h_j,$$
$$\phi_{\bar{\eta}} = \sum_j Z_{j4}^H h_j, \qquad \phi_s = \sum_j Z_{j5}^H h_j. \quad (25)$$

Other mass matrices can be found in Refs. [31,32].

Here, we show some of the couplings that we need in the $U(1)_X$SSM. We deduce the vertices of $Z - \tilde{e}_i - \tilde{e}_j^*$,

$$\mathcal{L}_{Z\tilde{e}\tilde{e}^*} = \frac{1}{2}\tilde{e}_j^*\Big[(g_2\cos\theta_W\cos\theta'_W - g_1\cos\theta'_W\sin\theta_W + g_{YX}\sin\theta'_W)\sum_{a=1}^{3}Z_{i,a}^{E,*}Z_{j,a}^E + ((2g_{YX} + g_X)\sin\theta'_W - 2g_1\cos\theta'_W\sin\theta_W) \times \sum_{a=1}^{3}Z_{i,3+a}^{E,*}Z_{j,3+a}^E\Big](p_i^\mu - p_j^\mu)\tilde{e}_i Z_\mu. \quad (26)$$

We also deduce the vertices of $\bar{l}_i - \chi_j^- - \tilde{\nu}_k^R(\tilde{\nu}_k^I)$,

$$\mathcal{L}_{\bar{l}\chi^-\tilde{\nu}^R} = \frac{1}{\sqrt{2}}\bar{l}_i\{U_{j2}^* Z_{ki}^{R*}Y_l^i P_L - g_2 V_{j1}Z_{ki}^{R*}P_R\}\chi_j^-\tilde{\nu}_k^R,$$
$$\mathcal{L}_{\bar{l}\chi^-\tilde{\nu}^I} = \frac{i}{\sqrt{2}}\bar{l}_i\{U_{j2}^* Z_{ki}^{I*}Y_l^i P_L - g_2 V_{j1}Z_{ki}^{I*}P_R\}\chi_j^-\tilde{\nu}_k^I. \quad (27)$$

The vertices of $\bar{\chi}_i^0 - l_j - \tilde{e}_k$ are

$$\mathcal{L}_{\bar{\chi}_i^0 l\tilde{e}} = \bar{\chi}_i^0\Big\{\Big(\frac{1}{\sqrt{2}}(g_1N_{i1}^* + g_2N_{i2}^* + g_{YX}N_{i5}^*)Z_{kj}^E - N_{i3}^*Y_l^j Z_{k3+j}^E\Big)P_L - \Big[\frac{1}{\sqrt{2}}(2g_1N_{i1} + (2g_{YX} + g_X)N_{i5})Z_{k3+a}^E + Y_l^j Z_{kj}^E N_{i3}\Big]P_R\Big\}l_j\tilde{e}_k. \quad (28)$$

To save space in the text, the remaining vertices can be found in Refs. [33,34,41,42].

III. Z BOSON DECAYS $Z \to l_i^\pm l_j^\mp$

In this section, we analyze the LFV processes $Z \to l_i^\pm l_j^\mp$. The corresponding Feynman diagrams can

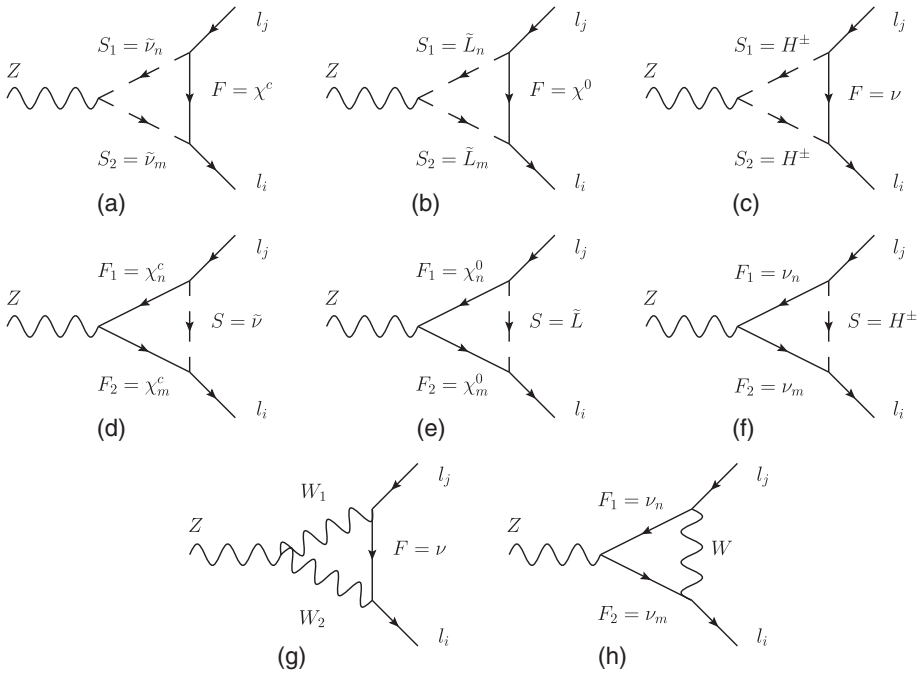

FIG. 1. Feynman diagrams for the $Z \to l_i^{\pm} l_j^{\mp}$ processes in the $U(1)_X$SSM. Note that F represents the Dirac (Majorana) fermion, S represents the scalar boson, and W represents the W boson.

be depicted by Figs. 1 and 2, and the corresponding effective amplitudes can be written as [43–45]

$$\mathcal{M}_\mu = \bar{l}_i \gamma_\mu (F_L P_L + F_R P_R) l_j, \tag{29}$$

with

$$F^Z_{L,R} = F_{L,R}(A) + F_{L,R}(W) + F_{L,R}(B). \tag{30}$$

The coefficients $F_{L,R}$ can be obtained from the amplitudes of the Feynman diagrams. Note that $F_{L,R}(A)$ corresponds to Figs. 1(a)–1(f), and it stands for the contributions from the chargino-sneutrino, the neutralino-slepton, and the neutrino-charged Higgs. Here, $F_{L,R}(W)$ corresponds to Figs. 1(g), 1(h) and stands for contributions from the W-neutrino due to three light neutrinos and three heavy neutrinos mixing together.

The contributions obtained from Figs. 1(a)–1(f) are expressed by $F_{L,R}(A) = F^{\alpha}_{L,R}(A)(\alpha = 1 \ldots 6)$. The specific forms are as follows:

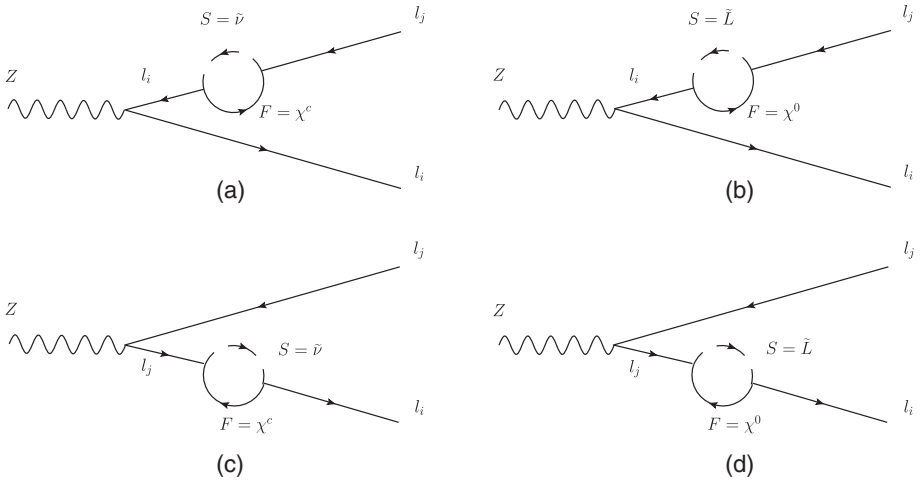

FIG. 2. Feynman diagrams for the processes $Z \to l_i^{\pm} l_j^{\mp}$ in the $U(1)_X$SSM, which denote self-energy diagrams contributing to $Z \to l_i^{\pm} l_j^{\mp}$ from loops.

$$F_L^{(1,2,3)}(A) = \frac{i}{2} H_R^{S_2 F \bar{l}_i} H^{Z S_1 S_2^*} H_L^{S_1^* l_j \bar{F}} G_2(x_F, x_{S_1}, x_{S_2}),$$
$$F_L^{(4,5,6)}(A) = \frac{i}{2}\left[\frac{2 m_{F_1} m_{F_2}}{m_W^2} H_R^{S F_2 \bar{l}_i} H_L^{Z F_1 \bar{F}_2} H_L^{S^* l_j \bar{F}_1} G_1 \times (x_S, x_{F_1}, x_{F_2}) - H_R^{S F_2 \bar{l}_i} H_R^{Z F_1 \bar{F}_2} H_L^{S^* l_j \bar{F}_1} \times G_2(x_S, x_{F_1}, x_{F_2})\right],$$
$$F_R^{\alpha}(A) = F_L^{\alpha}(A)|_{L \leftrightarrow R}, \qquad \alpha = 1 \ldots 6. \tag{31}$$

Here, $x_i = m_i^2/m_W^2$, with m_i representing the mass of the corresponding particle and m_W representing the energy scale of the NP. Their specific expressions are given in the Appendix. In Fig. 1(a), S_1 and S_2 represent a CP-even scalar neutrino and a CP-odd scalar neutrino, and F represents a chargino. Note that $H_R^{S_2 F \bar{l}_i}$ is the right-handed coupling of the vertex $\tilde{\nu}^{I(R)} - \chi^{\pm} - \bar{l}_i$, $H^{Z S_1 S_2^*}$ is the coupling of $\tilde{\nu}^{R(I)} - Z - \tilde{\nu}^{I(R)}$, and $H_L^{S_1^* l_j \bar{F}}$ is the left-handed coupling of the vertex $\tilde{\nu}^{R(I)} - \bar{\chi}^{\pm} - l_j$. The concrete forms of $H_R^{S_2 F \bar{l}_i}$, $H^{Z S_1 S_2^*}$, and $H_L^{S_1^* l_j \bar{F}}$ are shown in Eq. (A1) in the Appendix. In Fig. 1(b), S_1 and S_2 represent the scalar lepton $\tilde{L}$, and F denotes the neutralino χ^0. The couplings $H_R^{\tilde{L}_n \chi^0 \bar{l}_i}$, $H^{Z \tilde{L}_m \tilde{L}_n^*}$, and $H_L^{\tilde{L}_m^* l_j \bar{\chi}^0}$ are given in Eq. (A2) of the Appendix. In Fig. 1(c), S_1 and S_2 represent the charged Higgs $H^{\pm}$, and F denotes the neutrino ν. The couplings $H_R^{H^{\pm} \nu \bar{l}_i}$, $H^{Z H^{\pm} H^{\pm}}$, and $H_L^{H^{\pm} l_j \bar{\nu}}$ are given in Eq. (A3) of the Appendix.

In Fig. 1(d), F_1 and F_2 represent $\chi^{\pm}$, S denotes the CP-even (CP-odd) scalar neutrino $\tilde{\nu}^{R(I)}$, and m_{F_1} and m_{F_2} are the chargino masses. The concrete forms of the couplings of the chargino-scalar neutrino-lepton and the chargino-Z-chargino are collected in Eq. (A4) of the Appendix. In Fig. 1(e), F_1 and F_2 represent neutralinos, S denotes the scalar lepton, and m_{F_1} and m_{F_2} are the neutralino masses. The corresponding couplings are given in Eq. (A5) of the Appendix. In Fig. 1(f), F_1 and F_2 represent neutrinos, S denotes the charged Higgs, and m_{F_1} and m_{F_2} denote the neutrino masses. We show the couplings in Eq. (A6).

The specific forms of the one-loop functions $G_i(x_1, x_2, x_3)(i = 1 \ldots 3)$ are

$$G_1(x_1, x_2, x_3) = \frac{1}{16\pi^2}\left[\frac{x_1 \ln x_1}{(x_1 - x_2)(x_1 - x_3)} + \frac{x_2 \ln x_2}{(x_2 - x_1)(x_2 - x_3)} + \frac{x_3 \ln x_3}{(x_3 - x_1)(x_3 - x_2)}\right],$$
$$G_2(x_1, x_2, x_3) = \frac{1}{16\pi^2}\left[\frac{x_1^2 \ln x_1}{(x_1 - x_2)(x_1 - x_3)} + \frac{x_2^2 \ln x_2}{(x_2 - x_1)(x_2 - x_3)} + \frac{x_3^2 \ln x_3}{(x_3 - x_1)(x_3 - x_2)}\right]. \tag{32}$$

The contributions obtained from Figs. 1(g) and 1(h) are expressed by $F_{L,R}(W) = F_{L,R}^{\alpha}(W)$ ($\alpha = 1, 2$). The specific forms are as follows:

$$F_L^{(1,2)}(W) = i[3 H_L^{W_2 F \bar{l}_i} H^{Z W_1 W_2^*} H_L^{W_1^* l_j \bar{F}} G_2(x_F, x_{W_1}, x_{W_2}) - H_L^{W F_2 \bar{l}_i} H_L^{Z F_1 \bar{F}_2} H_L^{\bar{F}_1 l_j W^*} G_2(x_W, x_{F_1}, x_{F_2})],$$
$$F_R^{(1,2)}(W) = 0. \tag{33}$$

Here, $F(F_1, F_2)$ represents the neutrino. The required couplings of the W-Z-W, the lepton-neutrino-W, and the neutrino-Z-neutrino are collected in Eqs. (A7) and (A8) of the Appendix.

The contributions obtained from Fig. 2 are expressed by $F_{L,R}(B) = F_{L,R}^{\alpha}(B)(\alpha = 1 \ldots 4)$. The specific forms are as follows:

$$F_L^{(1,2)}(B) = \frac{H_L^{Z l_i \bar{l}_i}}{m_{l_j}^2 - m_{l_i}^2}\left\{I_1(x_F, x_S) + \frac{m_{l_j}^2}{m_W^2}[I_2(x_F, x_S) - I_3(x_F, x_S)](m_{l_j} m_F H_R^{S F \bar{l}_i} H_R^{S^* l_j \bar{F}} + m_{l_i} m_F H_L^{S F \bar{l}_i} H_L^{S^* l_j \bar{F}}) - \frac{1}{2} G_3(x_F, x_S)(m_{l_j}^2 H_R^{S F \bar{l}_i} H_L^{S^* l_j \bar{F}} + m_{l_i} m_{l_j} H_L^{S F \bar{l}_i} H_R^{S^* l_j \bar{F}})\right\},$$
$$F_L^{(3,4)}(B) = \frac{H_L^{Z l_j \bar{l}_j}}{m_{l_i}^2 - m_{l_j}^2}\left\{I_1(x_F, x_S) + \frac{m_{l_i}^2}{m_W^2}[I_2(x_F, x_S) - I_3(x_F, x_S)](m_{l_i} m_F H_R^{S F \bar{l}_i} H_R^{S^* l_j \bar{F}} + m_{l_j} m_F H_L^{S F \bar{l}_i} H_L^{S^* l_j \bar{F}}) - \frac{1}{2} G_3(x_F, x_S)(m_{l_i}^2 H_L^{S F \bar{l}_i} H_R^{S^* l_j \bar{F}} + m_{l_i} m_{l_j} H_R^{S F \bar{l}_i} H_L^{S^* l_j \bar{F}})\right\},$$
$$F_R^{\alpha}(B) = F_L^{\alpha}(B)|_{L \leftrightarrow R}, \quad \alpha = 1 \ldots 4. \tag{34}$$

Note that $H_L^{Zl_i\bar{l}_i} = H_L^{Zl_j\bar{l}_j} = \frac{i}{2}(-g_1 \cos\theta'_W \sin\theta_W + g_2 \cos\theta_W \cos\theta'_W + g_{YX} \sin\theta'_W)$ represents left-handed coupling of the lepton-Z-lepton. In Fig. 2(a), F and S denote the chargino and CP-even (CP-odd) scalar neutrino, and m_F represents the mass of the chargino. In Fig. 2(b), F and S denote the neutralino and scalar lepton, and m_F is the mass of the neutralino. The required couplings in Figs. 2(a) and 2(b) can be found from the couplings in Figs. 1(a) and 1(b). The conditions of Figs. 2(c) and 2(d) are similar to those of Figs. 2(a) and 2(b).

Here,

$$
\begin{aligned}
I_1(x_1,x_2) &= \frac{1}{16\pi^2}\left[\frac{1+\log x_2}{x_2-x_1} + \frac{x_1\log x_1 - x_2\log x_2}{(x_2-x_1)^2}\right],\\
I_2(x_1,x_2) &= \frac{1}{16\pi^2}\left[-\frac{1+\log x_2}{x_2-x_1} - \frac{x_1\log x_1 - x_2\log x_2}{(x_2-x_1)^2}\right],\\
G_3(x_1,x_2) &= -\frac{1}{16\pi^2}\left[\frac{x_2^2\log x_2 - x_1^2\log x_1}{(x_2-x_1)^2}\right.\\
&\quad \left. + \frac{x_2+2x_2\log x_2}{(x_1-x_2)} - \frac{1}{2}\right].
\end{aligned}
\tag{35}
$$

Then, the branching ratios of $Z \to l_i^{\pm} l_j^{\mp}$ are defined as

$$
\begin{aligned}
\mathrm{Br}(Z \to l_i^{\pm} l_j^{\mp}) &= \frac{1}{12\pi}\frac{m_Z}{\Gamma_Z}(|F_L^Z|^2 + |F_R^Z|^2)\\
&= \frac{1}{12\pi}\frac{m_Z}{\Gamma_Z}(|F_L(A) + F_L(W) + F_L(B)|^2\\
&\quad + |F_R(A) + F_R(B)|^2),
\end{aligned}
\tag{36}
$$

where Γ_Z represents the total decay width of the Z boson, $\Gamma_Z \simeq 2.4952$ GeV [16].

IV. HIGGS BOSON DECAYS $h \to l_i^{\pm} l_j^{\mp}$

In this section, we analyze the LFV processes $h \to l_i^{\pm} l_j^{\mp}$. The corresponding Feynman diagrams are depicted in Figs. 3 and 4.

The corresponding effective amplitude can be written as

$$
\mathcal{M} = \bar{l}_i(F_L P_L + F_R P_R) l_j h, \tag{37}
$$

with

$$
F_{L,R}^h = F_{L,R}(C) + F_{L,R}(D). \tag{38}
$$

The contribution given in Fig. 3 is expressed by $F_{L,R}(C) = F_{L,R}^{\alpha}(C)(\alpha = 1\ldots6)$. The specific forms are as follows:

$$
\begin{aligned}
F_L^{(1,2,3)}(C) &= \frac{m_F}{m_{N_p}^2} H^{hS_1S_2^*} H_L^{S_2F\bar{l}_i} H_L^{S_1^* l_j \bar{F}} G_1(x_F, x_{S_1}, x_{S_2}),\\
F_L^{(4,5,6)}(C) &= \frac{m_{F_1} m_{F_2}}{m_{N_p}^2} H_L^{SF_2\bar{l}_i} H_L^{hF_1\bar{F}_2} H_L^{S^* l_j \bar{F}_1} G_1(x_S, x_{F_1}, x_{F_2})\\
&\quad + H_L^{SF_2\bar{l}_i} H_R^{hF_1\bar{F}_2} H_L^{S^* l_j \bar{F}_1} G_2(x_S, x_{F_1}, x_{F_2}),\\
F_R^{\alpha}(C) &= F_L^{\alpha}(C)|_{L\leftrightarrow R}, \qquad \alpha = 1\ldots6.
\end{aligned}
\tag{39}
$$

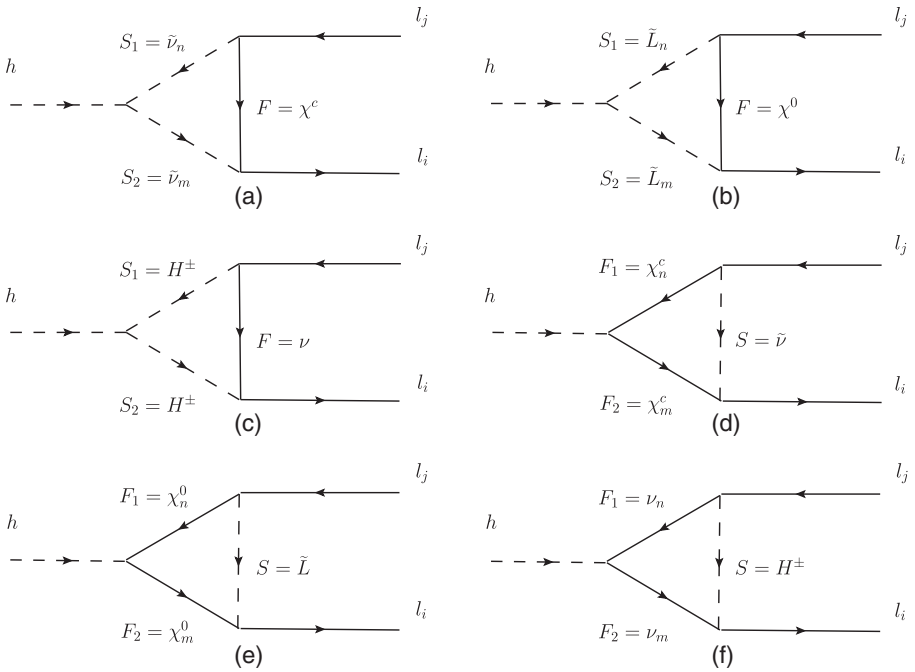

FIG. 3. Feynman diagrams for the processes $h \to l_i^{\pm} l_j^{\mp}$ in the $U(1)_X$SSM, which denote the contributions of vertex diagrams for $h \to l_i^{\pm} l_j^{\mp}$ from loops.

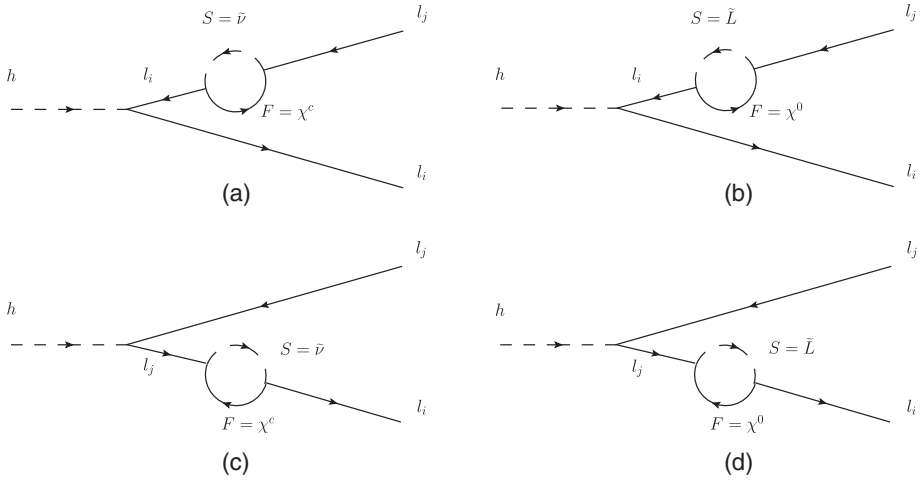

FIG. 4. Feynman diagrams for the processes $h \to l_i^{\pm} l_j^{\mp}$ in the $U(1)_X$SSM, which denote self-energy diagrams contributing to $h \to l_i^{\pm} l_j^{\mp}$ from loops.

Figures 3(a)–3(f) are similar to Figs. 1(a)–1(f), with Z replaced by h. So we just show the couplings relating to h. In Fig. 3(a), $H^{hS_1S_2^*} \to H^{h\tilde{\nu}^R\tilde{\nu}^{R*}}(H^{h\tilde{\nu}^I\tilde{\nu}^{I*}})$. The concrete form of $H^{h\tilde{\nu}^R\tilde{\nu}^{R*}}$ can be found in the Appendix [Eq. (A10)] of Ref. [33]. Note that $H^{h\tilde{\nu}^I\tilde{\nu}^{I*}}$ is very similar to $H^{h\tilde{\nu}^R\tilde{\nu}^{R*}}$, with the replacement $Z^R \to Z^I$.

In Fig. 3(b), S_1 and S_2 denote scalar leptons. Then $H^{hS_1S_2^*} \to H^{h\tilde{L}\tilde{L}^*}$, which reads as

$$\begin{aligned} H^{h\tilde{L}_n\tilde{L}_m^*} = \frac{i}{4}\Bigg\{ & \sum_{a=1}^{3} Z^{E,*}_{m,a} Z^{E}_{n,a} ((g_2^2 - g_{YX} g_X - g_1^2 - g_{YX}^2)(v_d Z^H_{b1} - v_u Z^H_{b2}) + g_{YX} g_X (v_{\bar{\eta}} Z^H_{b4} \\ & - v_\eta Z^H_{b3})) + \sum_{a=1}^{3} Z^{E,*}_{m,3+a} Z^{E}_{n,3+a} ((2g_1^2 + 2g_{YX}^2 + 3 g_{YX} g_X + g_X^2)(v_d Z^H_{b1} - v_u Z^H_{b2}) \\ & + 2(g_{YX} g_X + g_X^2)(-v_{\bar{\eta}} Z^H_{b4} + v_\eta Z^H_{b3})) + \left(\sum_{a=1}^{3} Z^{E,*}_{m,a} Z^{E}_{n,3+a} + \sum_{a=1}^{3} Z^{E,*}_{m,3+a} Z^{E}_{n,a} \right) \\ & \times [-2\sqrt{2} T_{e,a} Z^H_{b1} + Y_{e,a} (2(v_S \lambda_H + \sqrt{2}\mu) Z^H_{b2} + 2 v_u \lambda_H Z^H_{b5})] \Bigg\}. \end{aligned} \tag{40}$$

In Fig. 3(c), the scalar particle is a charged Higgs, and

$$\begin{aligned} H^{hS_1S_2^*} \to H^{hH_m^{\pm} H_n^{\pm *}} = \frac{i}{4}\{ & (-Z^H_{b2} Z^+_{m2} - Z^H_{b1} Z^+_{m1})([(g_{YX} + g_X)^2 + g_1^2 + g_2^2](v_u Z^+_{n2} + v_d Z^+_{n1}) + (g_2^2 - 2\lambda_H^2) \\ & \times (v_d Z^+_{n1} - v_u Z^+_{n2})) + (Z^H_{b2} Z^+_{m1} + Z^H_{b1} Z^+_{m2})([(g_{YX} + g_X)^2 - 2g_2^2 + g_1^2 + 2\lambda_H^2](v_u Z^+_{n1} \\ & + v_d Z^+_{n2})) - 2 Z^H_{b4} (Z^+_{m2} - Z^+_{m1})((g_{YX} g_X + g_X^2) v_{\bar{\eta}} (Z^+_{n2} + Z^+_{n1}) + \lambda_c v_\eta \lambda_H (Z^+_{n1} - Z^+_{n2})) \\ & + Z^H_{b3} (Z^+_{m2} + Z^+_{m1})((g_{YX} g_X + g_X^2)(v_\eta Z^+_{n1} - v_\eta Z^+_{n2}) + \lambda_c v_{\bar{\eta}} \lambda_H^* (Z^+_{n1} + Z^+_{n2})) \\ & + Z^H_{b5} (Z^+_{m2} + Z^+_{m1})(Z^+_{n2} + Z^+_{n1})(\sqrt{2} T_{\lambda,H} + 2\lambda_H (\kappa v_s + \sqrt{2} M_S + \sqrt{2}\mu + \lambda_H v_S))\}. \end{aligned} \tag{41}$$

In Fig. 3(d), $F_1(F_2)$ denotes the chargino, while $m_{F_1}(m_{F_2})$ represents the chargino mass. The corresponding couplings are

$$\begin{aligned} H_L^{hF_1\bar{F}_2} \to H_L^{h\chi_n^{\pm}\bar{\chi}_m^{\pm}} &= -\frac{i}{\sqrt{2}}(g_2 U^*_{m1} V^*_{n2} Z^H_{b2} + U^*_{m2}(g_2 V^*_{n1} Z^H_{b1} + \lambda_H V^*_{n2} Z^H_{b5})), \\ H_R^{hF_1\bar{F}_2} \to H_R^{h\chi_n^{\pm}\bar{\chi}_m^{\pm}} &= -\frac{i}{\sqrt{2}}(g_2 U_{n1} V_{m2} Z^H_{b2} + U_{n2}(g_2 V_{m1} Z^H_{b1} + \lambda_H^* V_{m2} Z^H_{b5})). \end{aligned} \tag{42}$$

In Fig. 3(e), $F_1(F_2)$ and $m_{F_1}(m_{F_2})$ represent the neutralino and neutralino mass, respectively. The Higgs coupling with neutralino $H^{h\chi^0\bar{\chi}^0}$ is shown in Eq. (A5) of the Appendix in our previous work [42]. In Fig. 3(f), F_1 and F_2 are neutrinos. The terms proportional to a tiny neutrino mass (m_{F_1}, m_{F_2}) are not of interest. We do not show the Higgs-neutrino-neutrino couplings because the corrections from Fig. 3(f) are very small.

The contributions obtained from Fig. 4 are expressed by $F_{L,R}(D) = F^{\alpha}_{L,R}(D)(\alpha = 1\ldots4)$. The specific forms are as follows:

$$
\begin{aligned}
F_L^{(1,2)}(D) &= \frac{H_L^{hl_i\bar{l}_i}}{m_{l_j}^2 - m_{l_i}^2}\Big\{ I_1(x_F, x_S) + \frac{m_{l_j}^2}{m_W^2}[I_2(x_F, x_S) - I_3(x_F, x_S)](m_{l_j} m_F H_R^{SF\bar{l}_i} H_R^{S^* l_j \bar{F}} + m_{l_i} m_F H_L^{SF\bar{l}_i} H_L^{S^* l_j \bar{F}}) \\
&\quad - \frac{1}{2} G_3(x_F, x_S)(m_{l_j}^2 H_R^{SF\bar{l}_i} H_L^{S^* l_j \bar{F}} + m_{l_i} m_{l_j} H_L^{SF\bar{l}_i} H_R^{S^* l_j \bar{F}})\Big\}, \\
F_L^{(3,4)}(D) &= \frac{H_L^{hl_j\bar{l}_j}}{m_{l_i}^2 - m_{l_j}^2}\Big\{ I_1(x_F, x_S) + \frac{m_{l_i}^2}{m_W^2}[I_2(x_F, x_S) - I_3(x_F, x_S)](m_{l_i} m_F H_R^{SF\bar{l}_i} H_R^{S^* l_j \bar{F}} + m_{l_j} m_F H_L^{SF\bar{l}_i} H_L^{S^* l_j \bar{F}}) \\
&\quad - \frac{1}{2} G_3(x_F, x_S)(m_{l_i}^2 H_L^{SF\bar{l}_i} H_R^{S^* l_j \bar{F}} + m_{l_i} m_{l_j} H_R^{SF\bar{l}_i} H_L^{S^* l_j \bar{F}})\Big\}, \\
F_R^{\alpha}(D) &= F_L^{\alpha}(D)|_{L \leftrightarrow R}, \quad \alpha = 1\ldots4.
\end{aligned} \tag{43}
$$

The lepton-h-lepton coupling is denoted by $H_L^{hl_i\bar{l}_i} = -\frac{i}{\sqrt{2}} Y_{e,i} Z_{b1}^H$. In Fig. 4, the other couplings and m_F are the same as the corresponding terms in Fig. 2.

Then, the branching ratio of $h \to l_i^{\pm} l_j^{\mp}$ is defined as

$$
\mathrm{Br}(h \to l_i^{\pm} l_j^{\mp}) = \frac{1}{16\pi} \frac{m_h}{\Gamma_h} (|F_L^h|^2 + |F_R^h|^2), \tag{44}
$$

where $\Gamma_h \simeq \Gamma_h^{\mathrm{SM}} \simeq 4.1 \times 10^{-3}$ GeV [46]. Note that Γ_h represents the total decay width of the Higgs boson in the $U(1)_X$SSM, and Γ_h^{SM} represents the predicted value of the 125 GeV Higgs boson total decay width in the SM. In the following section, we choose the supersymmetric particles in the $U(1)_X$SSM that are heavy and whose contributions to the decay width of the 125 GeV Higgs boson are weak. Hence, we choose Γ_h, which is approximately equal to Γ_h^{SM}.

V. NUMERICAL ANALYSIS

In this section, we study the numerical results and consider the experimental constraints from the lightest CP-even Higgs mass $m_{h^0} = 125.1$ GeV [3,4,47–50]. In order to obtain reasonable numerical results, we need to study some sensitive parameters and consider the effect of $l_j \to l_i \gamma$ on LFV. The limitation of $\mu \to e\gamma$ is the strongest, and other restrictions can be achieved if the limit of $\mu \to e\gamma$ is satisfied [31]. Then, to show the numerical results clearly, we discuss the processes of $Z \to e\mu$, $Z \to e\tau$, $Z \to \mu\tau$ and $h \to e\mu$, $h \to e\tau$, $h \to \mu\tau$ in six subsections. We draw the relation diagrams and scatter diagrams with different parameters. After analyzing these graphs and the experimental limits of the branching ratios, reasonable parameter spaces are found to explain LFV.

According to the latest LHC data [51–56], we take, for the scalar, a lepton mass greater than 700 GeV, a chargino mass greater than 1100 GeV, and a scalar quark mass greater than 1500 GeV. Here, $M_{Z'} > 5.1$ TeV is the latest experimental constraint on the mass of the added heavy vector boson Z' [47]. The upper bound of the ratio of the Z' mass to its gauge coupling, $M_{Z'}/g_X \geq 6$ TeV under 99% C.L., is given in Refs. [48,49]. Taking into account the constraint from LHC data, $\tan\beta_\eta < 1.5$ [50]. Combined with the above experimental requirements, we obtain abundant data, and we process the data to get interesting one-dimensional graphs and multidimensional scatter plots. Considering the above constraints in the first paragraph, we use the following parameters:

$$
\begin{aligned}
&g_X = 0.3, \quad g_{YX} = 0.1, \quad \lambda_H = 0.1, \quad \lambda_C = -0.2, \quad \sqrt{v_\eta^2 + v_{\bar{\eta}}^2} = 17 \text{ TeV}, \\
&\mu = M_{BL} = T_{\lambda_H} = T_{\lambda_C} = T_\kappa = 1 \text{ TeV}, \quad M_{BB'} = 0.4 \text{ TeV}, \quad \kappa = 0.1, \\
&l_W = B_\mu = B_S = 0.1 \text{ TeV}^2, \quad T_{Xii} = -1 \text{ TeV}, \quad Y_{Xii} = 1, \quad (i = 1, 2, 3).
\end{aligned} \tag{45}
$$

To simplify the numerical research, we use the relations for the parameters, and they vary in the following numerical analysis:

$$M^2_{\tilde{L}ij} = M^2_{\tilde{L}ji}, \qquad M^2_{\tilde{E}ij} = M^2_{\tilde{E}ji},$$
$$M^2_{\tilde{\nu}ij} = M^2_{\tilde{\nu}ji}, \qquad T_{eij} = T_{eji}, \qquad T_{\nu ij} = T_{\nu ji}(i \neq j). \quad (46)$$

Generally, the nondiagonal elements of the parameters are defined as zero unless noted otherwise.

A. $Z \to e\mu$

With the parameters $v_S = 4.3$ TeV, $M_1 = 1.2$ TeV, $M^2_{\tilde{L}ii} = 3$ TeV^2, $T_{eii} = 0.5$ TeV, $T_{\nu ii} = 1$ TeV, $M^2_{\tilde{\nu}ii} = 0.3$ TeV^2, and $M^2_{\tilde{E}ii} = 0.8$ TeV^2 $(i = 1, 2, 3)$, we give $\mathrm{Br}(Z \to e\mu)$ schematic diagrams affected by different parameters in Fig. 5. The gray area is the experimental limit that this process satisfies.

In Fig. 5(a), we plot $\mathrm{Br}(Z \to e\mu)$ versus $M^2_{\tilde{E}12}$, in which the dashed curve corresponds to $M_S = 1.5$ TeV and the solid line corresponds to $M_S = 1.2$ TeV. We can clearly see that the two lines increase with the increasing $M^2_{\tilde{E}12}$ in the range 10^3 GeV^2–5×10^4 GeV^2. The dashed curve is larger than the solid curve. The solid line and the dashed line are located in the gray area. In Fig. 5(b), we plot $\mathrm{Br}(Z \to e\mu)$ versus $M^2_{\tilde{L}12}$, where the dashed curve corresponds to $M_S = 1.5$ TeV and the solid line corresponds to $M_S = 1.2$ TeV. We can clearly see that the two lines increase with increasing $M^2_{\tilde{L}12}$ in the range 10^3 GeV^2–6×10^4 GeV^2. The dashed curve is also larger than the solid curve. Both the solid line and the dashed line are located in the gray area. In Fig. 5(c), we plot $\mathrm{Br}(Z \to e\mu)$ versus M_S, in which the dashed curve corresponds to $M^2_{\tilde{L}12} = 6 \times 10^3$ GeV^2 and the solid line corresponds to $M^2_{\tilde{L}12} = 5 \times 10^3$ GeV^2. We can clearly see that the two lines increase with increasing M_S in the range 1350 GeV–1450 GeV. The dashed curve is larger than the solid curve. The solid line and the dashed line are located in the gray area. The other fixed parameters are based on our previous work, especially for the LFV processes $l_j \to l_i\gamma$ [31,57] in the $U(1)_X$SSM. The constraint from $\mu \to e\gamma$ is strict. The other restrictions are relatively loose and easy to satisfy.

In summary, $M^2_{\tilde{E}12}$ and $M^2_{\tilde{L}12}$ are the flavor mixing parameters appearing in the mass matrices of the slepton, the CP-even sneutrino, and the CP-odd sneutrino. The mass for the super partner of the Higgs singlet S is denoted by M_S, included in the mass matrices of the Higgs and neutralino. Thus, the contributions can be influenced, to some extent, by the parameters $M^2_{\tilde{E}12}$, $M^2_{\tilde{L}12}$, and M_S. Note that $\mathrm{Br}(Z \to e\mu)$ increases as the parameters $M^2_{\tilde{E}12}$, $M^2_{\tilde{L}12}$, and M_S increase. In Fig. 5, the dashed line has a higher

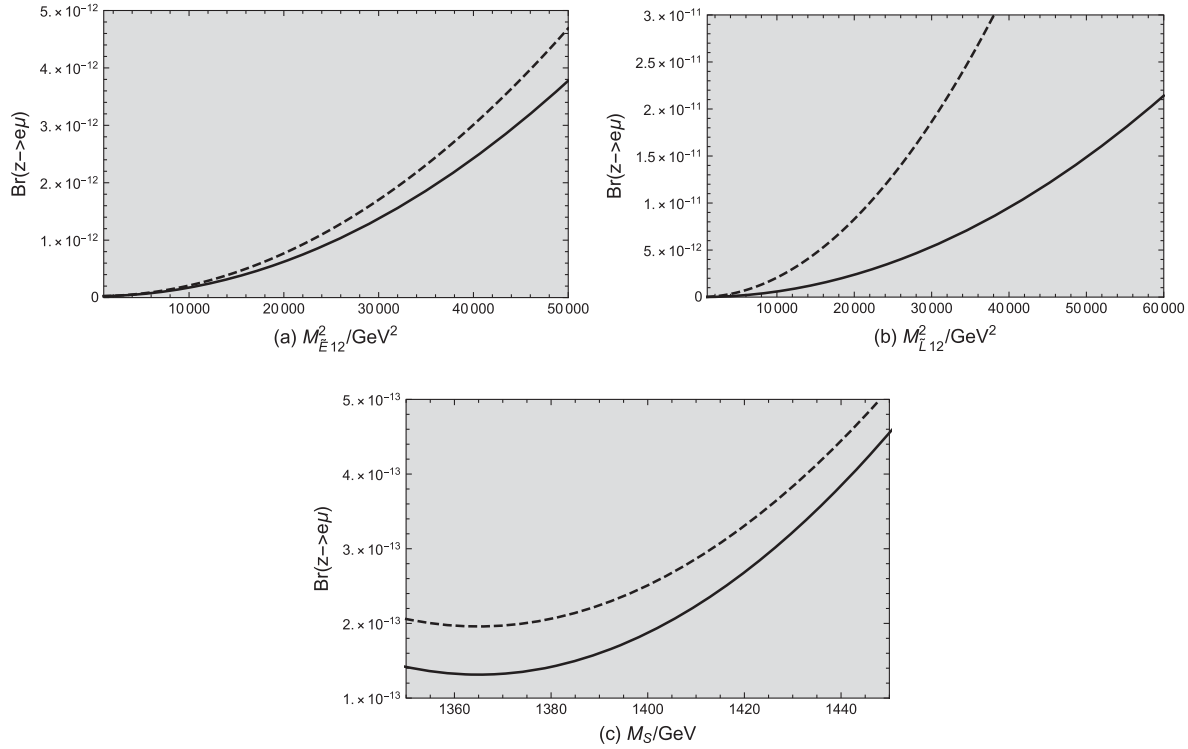

FIG. 5. The $\mathrm{Br}(Z \to e\mu)$ schematic diagrams affected by different parameters. The gray area is a reasonable value range where $\mathrm{Br}(Z \to e\mu)$ satisfies the upper limit. The dashed and solid lines in (a) and (b) correspond to $M_S = 1.5$ TeV and $M_S = 1.2$ TeV. The dashed and solid lines in (c) correspond to $M^2_{\tilde{L}12} = 6 \times 10^3$ GeV^2 and $M^2_{\tilde{L}12} = 5 \times 10^3$ GeV^2.

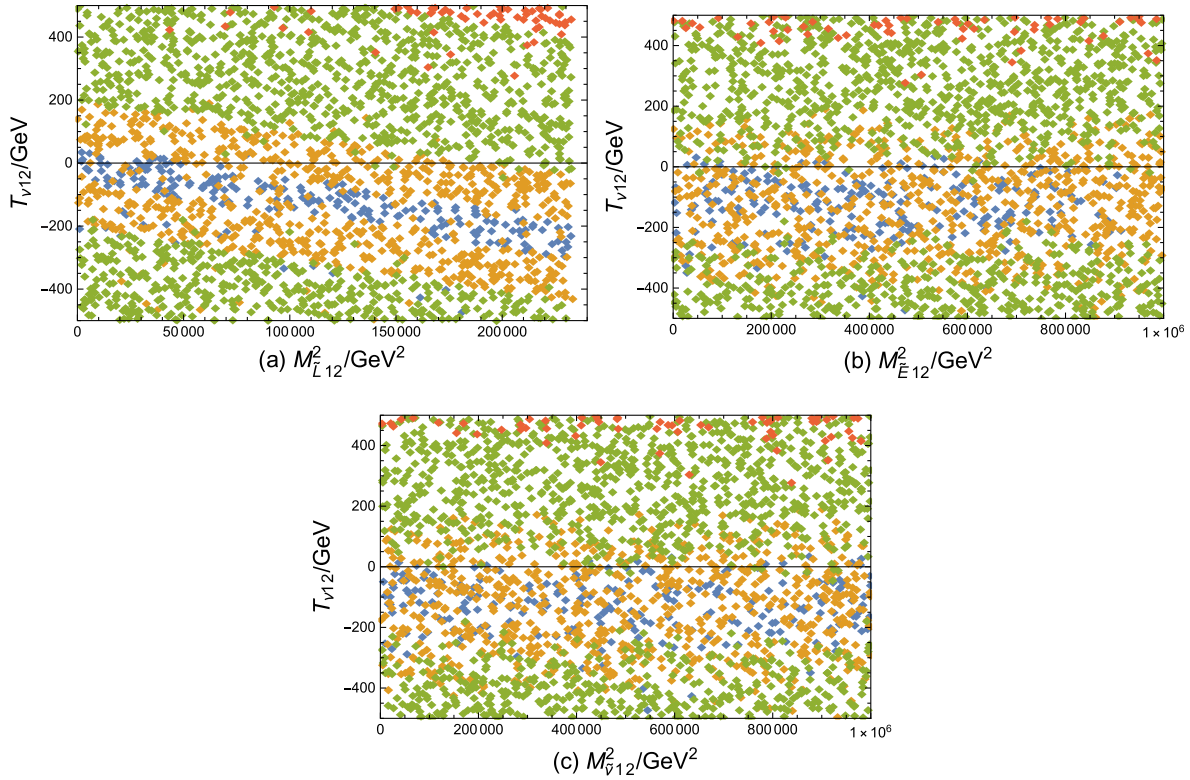

FIG. 6. Current limit on the lepton flavor violating decay $Z \to e\mu$. A reasonable parameter space is selected to scatter points, with blue $[0 < \mathrm{Br}(Z \to e\mu) < 5 \times 10^{-14}]$, yellow $[5 \times 10^{-14} \leq \mathrm{Br}(Z \to e\mu) < 5 \times 10^{-13}]$, green $[5 \times 10^{-13} \leq \mathrm{Br}(Z \to e\mu) < 5 \times 10^{-12}]$, and red $[5 \times 10^{-12} \leq \mathrm{Br}(Z \to e\mu) < 7.5 \times 10^{-7}]$.

slope than the solid line, and they vary in the region 10^{-13}–10^{-11} much smaller than the current limit. All in all, $M^2_{\tilde{E}12}$, $M^2_{\tilde{L}12}$, and M_S are sensitive parameters that have obvious effects on $\mathrm{Br}(Z \to e\mu)$.

Next, supposing $M_S = 1.2$ TeV, we randomly scan the parameters. All the parameters involved are expressed in tabular form. Figure 6 is obtained from the parameters shown in Table V. We use blue $[0 < \mathrm{Br}(Z \to e\mu) < 5 \times 10^{-14}]$, yellow $[5 \times 10^{-14} \leq \mathrm{Br}(Z \to e\mu) < 5 \times 10^{-13}]$, green $[5 \times 10^{-13} \leq \mathrm{Br}(Z \to e\mu) < 5 \times 10^{-12}]$, and red $[5 \times 10^{-12} \leq \mathrm{Br}(Z \to e\mu) < 7.5 \times 10^{-7}]$ to represent the results in different parameter spaces for the process $Z \to e\mu$.

The relationship between $M^2_{\tilde{L}12}$ and $T_{\nu 12}$ is shown in Fig. 6(a). We can see that the overall change trend of scattered points is obvious in Fig. 6(a), where four types of points are concentrated in -500 GeV $< T_{\nu 12} < 500$ GeV. The blue parts are mainly in the range -300 GeV $< T_{\nu 12} < 50$ GeV, yellow parts are mainly in -400 GeV $< T_{\nu 12} < 200$ GeV, green parts are mainly in -500 GeV $< T_{\nu 12} < -200$ GeV and 0 GeV $< T_{\nu} < 500$ GeV, and red parts are mainly in 450 GeV $< T_{\nu 12} < 500$ GeV.

The relationship between $M^2_{\tilde{E}12}$ and $T_{\nu 12}$ is shown in Fig. 6(b). The relationship between $M^2_{\tilde{\nu}12}$ and $T_{\nu 12}$ is shown in Fig. 6(c). In Figs. 6(b) and 6(c), we find that the variation trend of scattered points is weak, where blue parts are mainly in the range -200 GeV $< T_{\nu 12} < 0$ GeV, yellow parts are mainly in -380 GeV $< T_{\nu 12} < 100$ GeV, green parts are mainly in -500 GeV $< T_{\nu 12} < -300$ GeV and 0 GeV $< T_{\nu 12} < 500$ GeV, and red parts are mainly in 400 GeV $< T_{\nu 12} < 500$ GeV.

TABLE V. Scanning parameters for Figs. 6 and 11, with $i = 1, 2, 3$.

Parameters	Min	Max
$M^2_{\tilde{L}12}$/GeV^2	0	10^6
$M^2_{\tilde{E}12}$/GeV^2	0	10^6
$M^2_{\tilde{\nu}12}$/GeV^2	0	10^6
T_{e12}/GeV	-300	300
$T_{\nu 12}$/GeV	-500	500
$M^2_{\tilde{L}ii}$/GeV^2	2×10^5	10^9
$M^2_{\tilde{E}ii}$/GeV^2	2×10^5	10^9
$M^2_{\tilde{\nu}ii}$/GeV^2	1×10^5	10^9
T_{eii}/GeV	-3000	3000
$T_{\nu ii}$/GeV	-3000	3000
$\tan\beta$	1	50
M_1/GeV	200	3000
M_2/GeV	600	3000

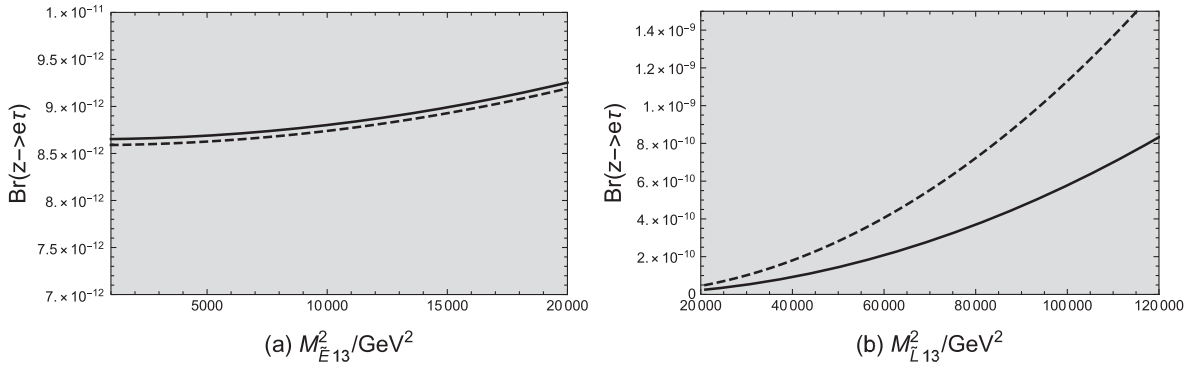

FIG. 7. The $\mathrm{Br}(Z \to e\tau)$ schematic diagrams affected by different parameters. The gray area is a reasonable value range, where $\mathrm{Br}(Z \to e\tau)$ satisfies the upper limit. The dashed and solid lines in (a) and (b) correspond to $M^2_{\tilde{L}ii} = 2.5 \times 10^6$ GeV^2 and $M^2_{\tilde{L}ii} = 3 \times 10^6$ GeV^2 with $i = 1, 2, 3$.

B. $Z \to e\tau$

With the parameters $v_S = 4.3$ TeV, $M_S = 1.2$ TeV, $\tan\beta = 20$, $T_{eii} = 2$ TeV, and $T_{\nu ii} = 3$ TeV $(i = 1, 2, 3)$, we show $\mathrm{Br}(Z \to e\tau)$ schematic diagrams affected by different parameters in Fig. 7. Identically, the gray area is the experimental limit that this process satisfies.

We study the branching ratio of $Z \to e\tau$ versus $M^2_{\tilde{E}13}$ with $M^2_{\tilde{L}ii} = 2.5 \times 10^6$ GeV^2$(3 \times 10^6$ GeV$^2)$ $(i = 1, 2, 3)$. In Fig. 7(a), the results are plotted with the dotted line and solid line, respectively, which almost overlap. Both lines increase with $M^2_{\tilde{E}13}$ increasing from 10^3 GeV^2 to 2×10^4 GeV^2, which indicates that $M^2_{\tilde{E}13}$ is a sensitive parameter for the numerical results. The solid and dashed lines are located in the gray area. In Fig. 7(b), we plot $Z \to e\tau$ versus $M^2_{\tilde{L}13}$, in which the dashed curve corresponds to $M^2_{\tilde{L}ii} = 2.5 \times 10^6$ GeV^2 and the solid line corresponds to $M^2_{\tilde{L}ii} = 3 \times 10^6$ GeV^2 $(i = 1, 2, 3)$. The dashed curve is larger than the solid curve. We can clearly see that the two lines increase with increasing $M^2_{\tilde{L}13}$ in the range of 2×10^3 GeV^2 to 1.2×10^4 GeV^2. The solid and dashed lines are located in the gray area. Thus, the contributions can be influenced by the parameters $M^2_{\tilde{E}13}$ and $M^2_{\tilde{L}13}$.

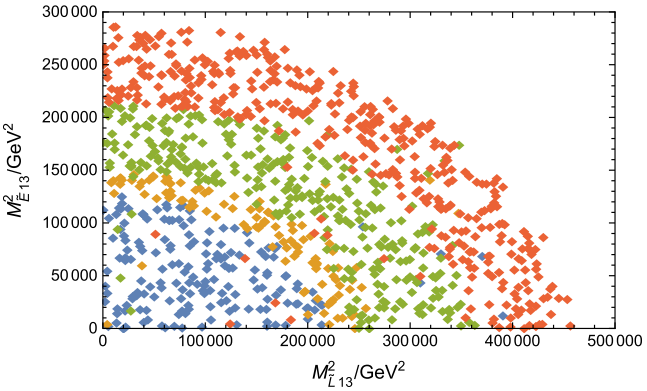

FIG. 8. Current limit on lepton flavor violating decay $Z \to e\tau$. Reasonable parameter space is selected to scatter points, with blue $[0 < \mathrm{Br}(Z \to e\tau) < 7 \times 10^{-15}]$, yellow $[7 \times 10^{-15} \leq \mathrm{Br}(Z \to e\tau) < 1 \times 10^{-14}]$, green $[1 \times 10^{-14} \leq \mathrm{Br}(Z \to e\tau) < 2 \times 10^{-14}]$, and red $[2 \times 10^{-14} \leq \mathrm{Br}(Z \to e\tau) < 9.8 \times 10^{-6}]$.

Next, supposing $M_S = 1.2$ TeV, we randomly scan the parameters. We scatter points on $Z \to e\tau$ in Fig. 8. Some parameter ranges of $\tan\beta$, M_1, M_2, $M^2_{\tilde{L}ii}$, $M^2_{\tilde{E}ii}$, $M^2_{\tilde{\nu}ii}$, T_{eii}, and $T_{\nu ii}$ $(i = 1, 2, 3)$ are given in Table V. In addition, other parameter spaces are also represented in Table VI. We use blue $[0 < \mathrm{Br}(Z \to e\tau) < 7 \times 10^{-15}]$, yellow $[7 \times 10^{-15} \leq \mathrm{Br}(Z \to e\tau) < 1 \times 10^{-14}]$, green $[1 \times 10^{-14} \leq \mathrm{Br}(Z \to e\tau) < 2 \times 10^{-14}]$, and red $[2 \times 10^{-14} \leq \mathrm{Br}(Z \to e\tau) < 9.8 \times 10^{-6}]$ to represent the results in different parameter spaces for the process of $Z \to e\tau$.

The analysis of the relationship between $M^2_{\tilde{L}13}$ and $M^2_{\tilde{E}13}$ is shown in Fig. 8. All the points are arranged in an arc in Fig. 8. We can see that the overall change trend of scattered points is obvious, where four types of points are concentrated in 0 GeV^2 $< M^2_{\tilde{E}13} < 3 \times 10^5$ GeV^2. The blue parts are mainly in the ranges 0 GeV^2 $< M^2_{\tilde{L}13} < 2.2 \times 10^5$ GeV^2 and 0 GeV^2 $< M^2_{\tilde{E}13} < 1.25 \times 10^5$ GeV^2, yellow parts are mainly in 2.2×10^5 GeV^2 $< M^2_{\tilde{L}13} < 2.6 \times 10^5$ GeV^2 and 1.25×10^5 GeV^2 $< M^2_{\tilde{E}13} < 1.5 \times 10^5$ GeV^2, green parts are mainly in 2.6×10^5 GeV^2 $< M^2_{\tilde{L}13} < 3.6 \times 10^5$ GeV^2 and 1.5×10^5 GeV^2 $< M^2_{\tilde{E}13} < 2.1 \times 10^5$ GeV^2, and red parts are mainly in 3.6×10^5 GeV^2 $< M^2_{\tilde{L}13} < 4.6 \times 10^5$ GeV^2 and 2.1×10^5 GeV^2 $< M^2_{\tilde{E}13} < 3 \times 10^5$ GeV^2.

TABLE VI. Scanning parameters for Figs. 8 and 13.

Parameters	Min	Max
$M^2_{\tilde{L}13}$/GeV^2	0	10^6
$M^2_{\tilde{E}13}$/GeV^2	0	10^6
$M^2_{\tilde{\nu}13}$/GeV^2	0	10^6
T_{e13}/GeV	−300	300
$T_{\nu 13}$/GeV	−500	500

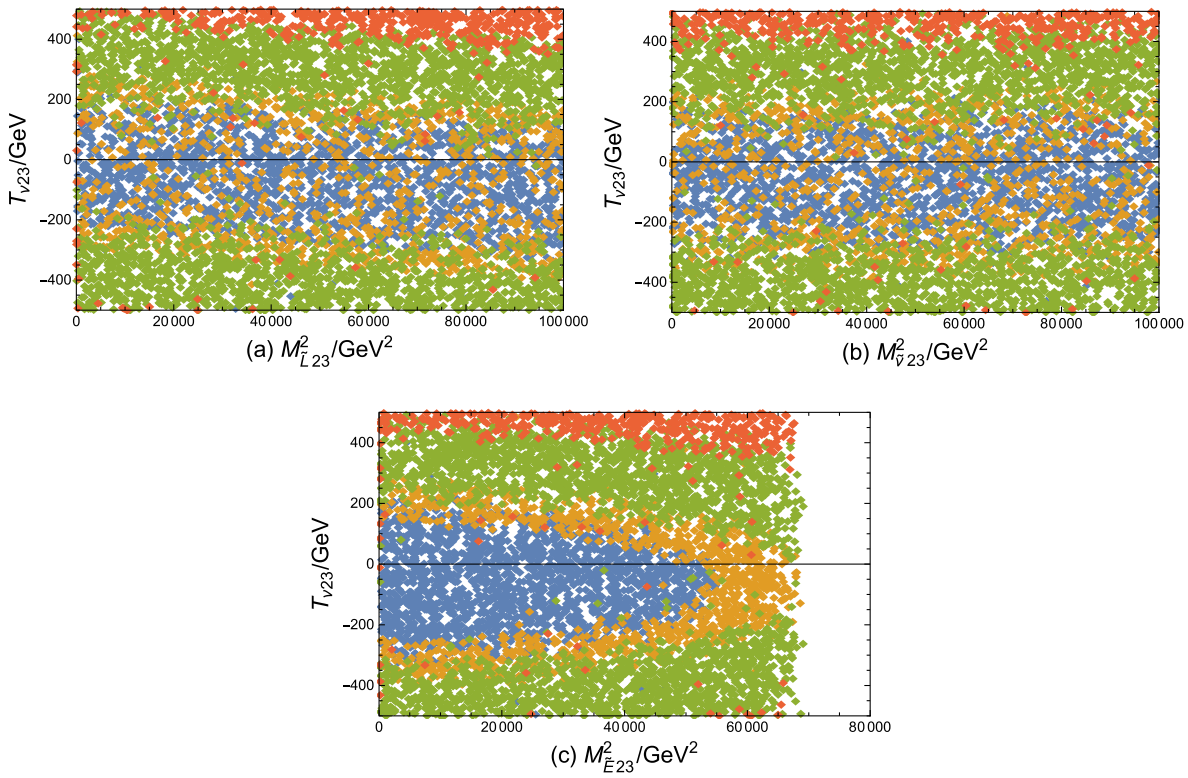

FIG. 9. Current limit on lepton flavor violating decay $Z \to \mu\tau$. Reasonable parameter space is selected to scatter points, with blue $[0 < \mathrm{Br}(Z \to \mu\tau) < 6 \times 10^{-13}]$, yellow $[6 \times 10^{-13} \leq \mathrm{Br}(Z \to \mu\tau) < 10^{-12}]$, green $[10^{-12} \leq \mathrm{Br}(Z \to \mu\tau) < 3 \times 10^{-12}]$, and red $[3 \times 10^{-12} \leq \mathrm{Br}(Z \to \mu\tau) < 1.2 \times 10^{-5}]$.

C. $Z \to \mu\tau$

The experimental upper bound for the LFV process $Z \to \mu\tau$ is 1.2×10^{-5}, which is about 1 order of magnitude larger than the process $Z \to e\mu$. The contributions from the neutralino-slepton and chargino-sneutrino can be influenced by the parameters $M^2_{\tilde{E}23}$, $M^2_{\tilde{L}23}$, and $T_{\nu 23}$. Through experimental analysis, we find that the law of the $Z \to \mu\tau$ process is similar to those of the $Z \to e\mu$ and $Z \to e\tau$ processes. The branching ratios increase with the increase of variables $M^2_{\tilde{E}23}$, $M^2_{\tilde{L}23}$, and $T_{\nu 23}$. When $M^2_{\tilde{E}23}$ is the variable, the branching ratio of $Z \to \mu\tau$ can reach 10^{-13}. When $M^2_{\tilde{L}23}$ is the variable, the branching ratio of $Z \to \mu\tau$ can reach 10^{-11}. When $T_{\nu 23}$ is the variable, the branching ratio of $Z \to \mu\tau$ can reach 10^{-9}. It can be deduced that the parameter $T_{\nu 23}$ is more sensitive than the parameters $M^2_{\tilde{E}23}$ and $M^2_{\tilde{L}23}$.

Next, we scatter points on $Z \to \mu\tau$ in Fig. 9 with the parameters in Table VII. These points are divided into blue $[0 < \mathrm{Br}(Z \to \mu\tau) < 6 \times 10^{-13}]$, yellow $[6 \times 10^{-13} \leq \mathrm{Br}(Z \to \mu\tau) < 10^{-12}]$, green $[10^{-12} \leq \mathrm{Br}(Z \to \mu\tau) < 3 \times 10^{-12}]$, and red $[3 \times 10^{-12} \leq \mathrm{Br}(Z \to \mu\tau) < 1.2 \times 10^{-5}]$ to represent the results in different parameter spaces for the process of $Z \to \mu\tau$.

The analysis of the relationship between $M^2_{\tilde{L}23}$ and $T_{\nu 23}$, $M^2_{\tilde{\nu}23}$ and $T_{\nu 23}$, and $M^2_{\tilde{E}23}$ and $T_{\nu 23}$ is shown in Fig. 9, where we can see four of these points concentrated in -500 GeV $< T_{\nu 23} < 500$ GeV. In Fig. 9(a), the blue parts are mainly in -300 GeV $< T_{\nu 23} < 180$ GeV, yellow parts are mainly in -400 GeV $< T_{\nu 23} < 200$ GeV, green parts are mainly in -500 GeV $< T_{\nu 23} < -200$ GeV and 200 GeV $< T_{\nu 23} < 400$ GeV, and red parts are mainly in 400 GeV $< T_{\nu 23} < 500$ GeV. In Fig. 9(b), the blue parts are mainly in -200 GeV $< T_{\nu 23} < 180$ GeV, yellow parts are mainly in -400 GeV $< T_{\nu 23} < 200$ GeV, green parts are mainly in -500 GeV $< T_{\nu 23} < -200$ GeV and 200 GeV $< T_{\nu 23} < 400$ GeV, and red parts are mainly in

TABLE VII. Scanning parameters for Fig. 9 with $i = 1, 2, 3$.

Parameters	Min	Max
$M^2_{\tilde{L}23}$/GeV^2	0	10^5
$M^2_{\tilde{E}23}$/GeV^2	0	10^5
$M^2_{\tilde{\nu}23}$/GeV^2	0	10^5
T_{e23}/GeV	-300	300
$T_{\nu 23}$/GeV	-500	500
$M^2_{\tilde{L}ii}$/GeV^2	2×10^5	10^8
$M^2_{\tilde{E}ii}$/GeV^2	2×10^5	10^8
$M^2_{\tilde{\nu}ii}$/GeV^2	1×10^5	10^8
T_{eii}/GeV	-3000	3000
$T_{\nu ii}$/GeV	-3000	3000

400 GeV $< T_{\nu 23} <$ 500 GeV. We find that the change trends in Figs. 9(a) and 9(b) are relatively weak, but Fig. 9(a) is relatively obvious compared to Fig. 9(b).

Finally, we analyze the effect from parameters $M^2_{\tilde{E}23}$ and $T_{\nu 23}$ in Fig. 9(c). The blue parts are almost symmetrically distributed about $T_{\nu 23} = 0$ and are concentrated in the range -200 GeV $< T_{\nu 23} < 200$ GeV and 0 GeV$^2 < M^2_{\tilde{E}23} < 5.5 \times 10^4$ GeV^2. The yellow parts are mainly distributed outside the green parts. The green parts are mainly in -500 GeV $< T_{\nu 23} < -300$ GeV and 200 GeV $< T_{\nu 23} <$ 400 GeV, and the red parts are mainly in 400 GeV $< T_{\nu 23} <$ 500 GeV.

D. $h \to e\mu$

In this subsection, we mainly analyze 125 GeV Higgs boson decays with LFV $h \to e\mu$ in the $U(1)_X$SSM. With the same parameters as the $Z \to e\mu$ process, we show $\mathrm{Br}(h \to e\mu)$ schematic diagrams affected by different parameters in Fig. 10.

In Fig. 10(a), we plot $\mathrm{Br}(h \to e\mu)$ versus $M^2_{\tilde{E}12}$, in which the numerical results are shown by the dashed and solid curves corresponding to $M_S = 1.5$ TeV and $M_S = 1.2$ TeV, respectively. Note that $\mathrm{Br}(h \to e\mu)$ varies with $M^2_{\tilde{E}12}$ in the range from 0 GeV^2 to 5×10^4 GeV^2. It can be clearly seen that both the solid line and the dashed line have an upward trend. The rising trend of the dashed line is greater than that of the solid line. The gray region represents the experimental limit. The dashed line in the range of 0 GeV^2 to 2×10^4 GeV^2 and the solid line in the range of 0 GeV^2 to 4×10^4 GeV^2 are in the gray area.

In Fig. 10(b), we plot $\mathrm{Br}(h \to e\mu)$ versus $M^2_{\tilde{L}12}$, in which the dashed line corresponds to $M_S = 1.5$ TeV and the solid line corresponds to $M_S = 1.2$ TeV. We can clearly see that the dashed line increases with the increasing $M^2_{\tilde{L}12}$ in the range of 0 GeV^2 to 2×10^4 GeV^2. The solid line increases with the increasing $M^2_{\tilde{L}12}$ in the range of 0 GeV^2 to 5×10^4 GeV^2. The dashed line is also larger than the solid line. The solid and dashed lines are located in the gray area. Thus, the contributions can obviously be influenced by the parameters $M^2_{\tilde{E}12}$ and $M^2_{\tilde{L}12}$.

Note that $\mathrm{Br}(h \to e\mu)$ versus M_S is plotted in Fig. 10(c), where the dashed line corresponds to $M^2_{\tilde{L}12} = 6 \times 10^3$ GeV^2 and the solid line corresponds to $M^2_{\tilde{L}12} = 5 \times 10^3$ GeV^2. It is clear that both the dashed and the solid line are increasing functions of M_S in the range of 1350 GeV to 1450 GeV. The dashed line is also larger than the solid line. Both lines reach 3.0×10^{-5} and are located in the gray area. If $M^2_{\tilde{E}12}$ and $M^2_{\tilde{L}12}$ are very small, $\mathrm{Br}(h \to e\mu)$ quickly becomes small, and the reasonable range of M_S becomes large.

Supposing $M_S = 1.2$ TeV and $M_1 = 1.2$ TeV, we randomly scan the parameters. These parameter ranges are

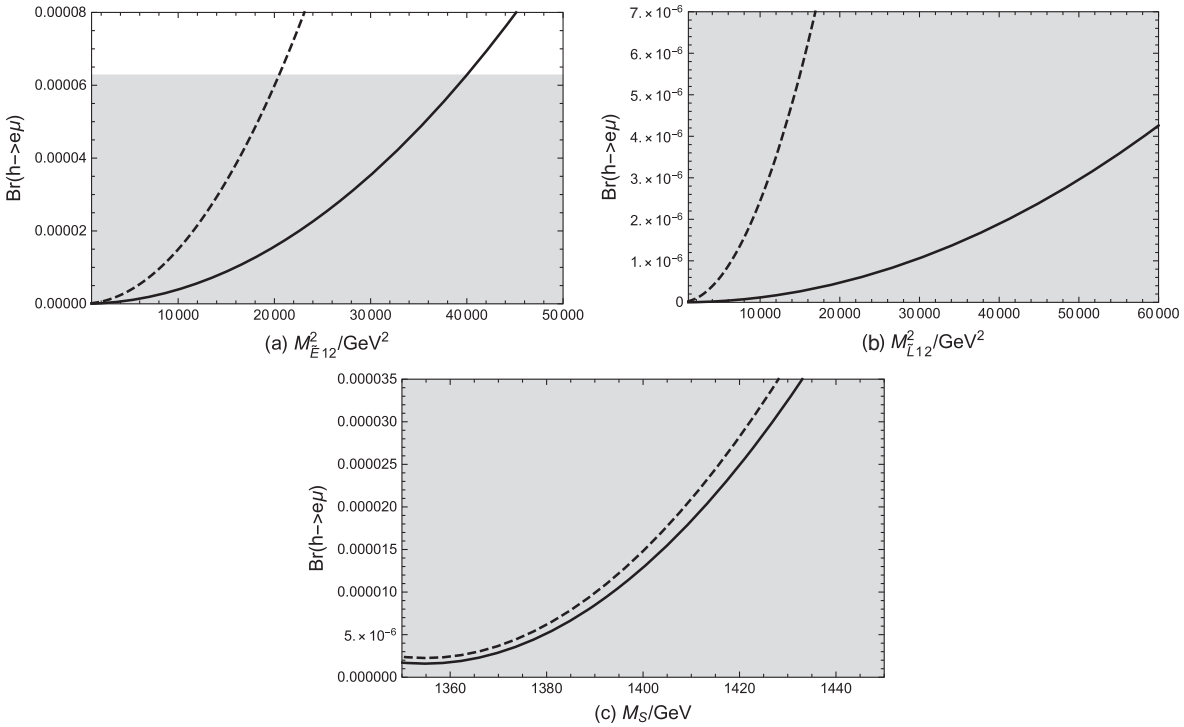

FIG. 10. The $\mathrm{Br}(h \to e\mu)$ schematic diagrams affected by different parameters. The gray area is a reasonable value range, where $\mathrm{Br}(h \to e\mu)$ satisfies the upper limit. The dashed and solid lines in (a) and (b) correspond to $M_S = 1.5$ TeV and $M_S = 1.2$ TeV. The dashed and solid lines in (c) correspond to $M^2_{\tilde{L}12} = 6 \times 10^3$ GeV^2 and $M^2_{\tilde{L}12} = 5 \times 10^3$ GeV^2.

given in Table V, thus obtaining Fig. 11. We use blue $[0 < \mathrm{Br}(h \to e\mu) < 2 \times 10^{-5}]$, yellow $[2 \times 10^{-5} \leq \mathrm{Br}(h \to e\mu) < 3 \times 10^{-5}]$, green $[3 \times 10^{-5} \leq \mathrm{Br}(h \to e\mu) < 5 \times 10^{-5}]$, and red $[5 \times 10^{-5} \leq \mathrm{Br}(h \to e\mu) < 6.28 \times 10^{-5}]$ to represent the results in different parameter spaces for the process $Z \to e\mu$.

The relationship between $M^2_{\tilde{L}12}$ and $M^2_{\nu 12}$ is shown in Fig. 11(a), and the relationship between $M^2_{\tilde{L}12}$ and $T_{\nu 12}$ is shown in Fig. 11(b). All points are clearly distributed in their respective regions. The four types of points are concentrated in $0\ \mathrm{GeV}^2 < M^2_{\tilde{L}12} < 2.3 \times 10^5\ \mathrm{GeV}^2$. The blue parts are mainly in $0\ \mathrm{GeV}^2 < M^2_{\tilde{L}12} < 1.3 \times 10^5\ \mathrm{GeV}^2$, yellow parts are mainly in $1.3 \times 10^5\ \mathrm{GeV}^2 < M^2_{\tilde{L}12} < 1.6 \times 10^5\ \mathrm{GeV}^2$, green parts are mainly in $1.6 \times 10^5\ \mathrm{GeV}^2 < M^2_{\tilde{L}12} < 2.1 \times 10^5\ \mathrm{GeV}^2$ GeV, and red parts are mainly in $2.1 \times 10^5\ \mathrm{GeV}^2 < M^2_{\tilde{L}12} < 2.3 \times 10^5\ \mathrm{GeV}^2$.

E. $h \to e\tau$

In this section, we analyze the 125 GeV Higgs boson decay $h \to e\tau$ in the $U(1)_X$SSM model. With the same parameters as the $Z \to e\tau$ process, we show $\mathrm{Br}(h \to e\tau)$ schematic diagrams affected by different parameters in Fig. 12.

Setting $v_S = 4.3$ TeV, we plot $\mathrm{Br}(h \to e\tau)$ versus $M^2_{\tilde{E}13}$ in Fig. 12(a). The dashed line corresponds to $M^2_{\tilde{L}ii} = 2.5 \times 10^6\ \mathrm{GeV}^2$, and the solid line corresponds to $M^2_{\tilde{L}ii} = 3 \times 10^6\ \mathrm{GeV}^2$ $(i = 1, 2, 3)$. We can clearly see that the two lines increase with increasing $M^2_{\tilde{E}13}$ in the range of $0\ \mathrm{GeV}^2 - 2 \times 10^4\ \mathrm{GeV}^2$. The dashed line is larger than the solid line. The solid line part in $0\ \mathrm{GeV}^2 < M^2_{\tilde{E}13} < 1.96 \times 10^4\ \mathrm{GeV}^2$ is in the gray area, and the dashed line part in $0\ \mathrm{GeV}^2 < M^2_{\tilde{E}13} < 1.9 \times 10^4\ \mathrm{GeV}^2$ is in the gray area. That is to say, the dashed and solid lines exceed the gray area.

In Fig. 12(b), we show $h \to e\tau$ versus $M^2_{\tilde{L}13}$, where the dashed line corresponds to $M^2_{\tilde{L}ii} = 2.5 \times 10^6\ \mathrm{GeV}^2$ and the solid line corresponds to $M^2_{\tilde{L}ii} = 3 \times 10^6\ \mathrm{GeV}^2$ $(i = 1, 2, 3)$. During $2 \times 10^3\ \mathrm{GeV}^2 < M^2_{\tilde{L}13} < 1.2 \times 10^5\ \mathrm{GeV}^2$, both the dashed line and the solid line are increasing functions, and the slope of the dashed line is greater than that of the solid line. The solid line part as a

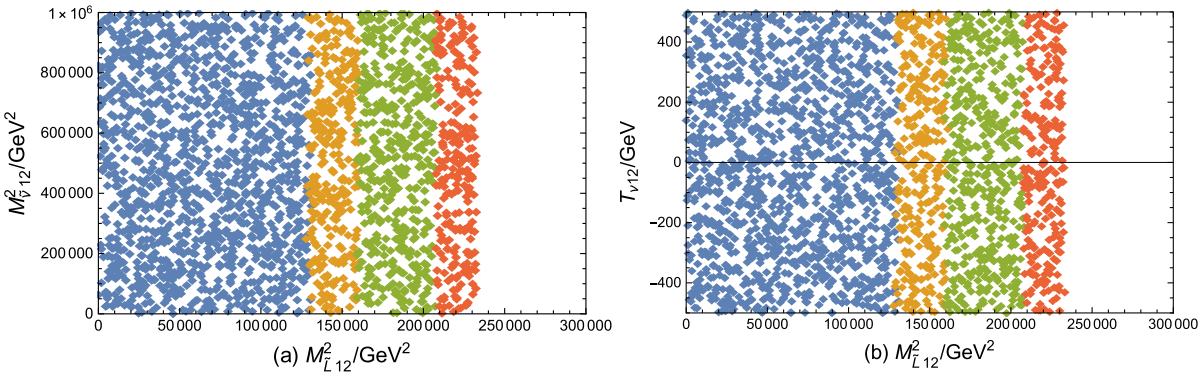

FIG. 11. Current limit on lepton flavor violating decay $h \to e\mu$. A reasonable parameter space is selected to scatter points, with blue $[0 < \mathrm{Br}(h \to e\mu) < 2 \times 10^{-5}]$, yellow $[2 \times 10^{-5} \leq \mathrm{Br}(h \to e\mu) < 3 \times 10^{-5}]$, green $[3 \times 10^{-5} \leq \mathrm{Br}(h \to e\mu) < 5 \times 10^{-5}]$, and red $[5 \times 10^{-5} \leq \mathrm{Br}(h \to e\mu) < 6.28 \times 10^{-5}]$.

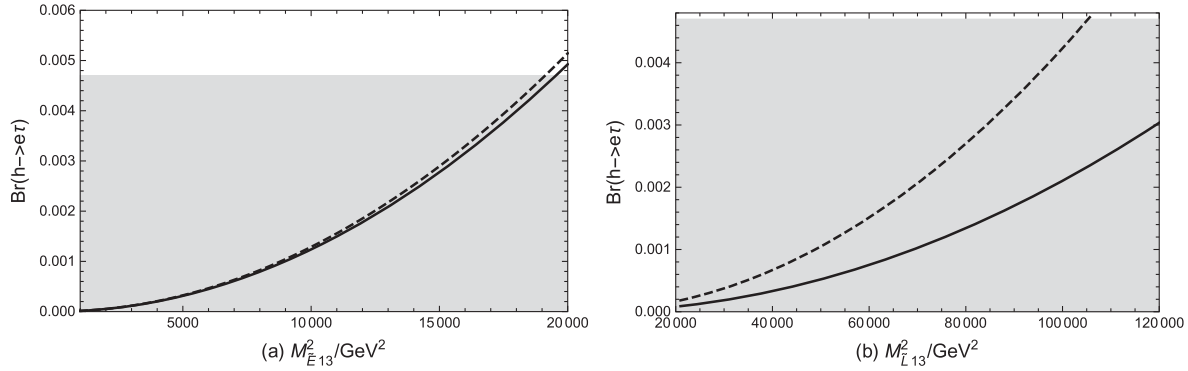

FIG. 12. The $\mathrm{Br}(h \to e\tau)$ schematic diagrams affected by different parameters. The gray area is a reasonable value range, where $\mathrm{Br}(Z \to e\tau)$ satisfies the upper limit. The dashed and solid lines in (a) and (b) correspond to $M^2_{\tilde{L}ii} = 2.5 \times 10^6\ \mathrm{GeV}^2$ and $M^2_{\tilde{L}ii} = 3 \times 10^6\ \mathrm{GeV}^2$ with $i = 1, 2, 3$.

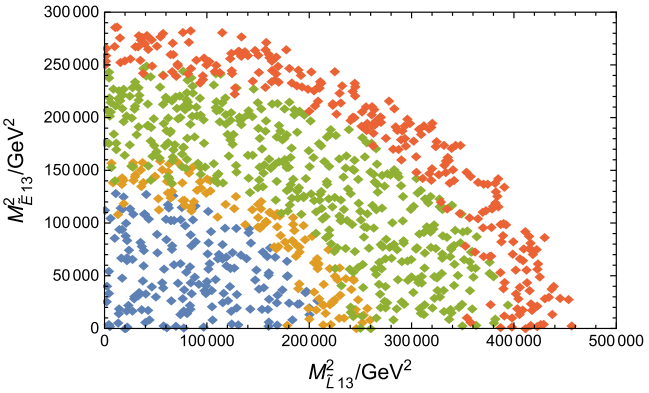

FIG. 13. Current limit on lepton flavor violating decay $h \to e\tau$. A reasonable parameter space is selected to scatter points, with blue $[0 < \mathrm{Br}(h \to e\tau) < 10^{-3}]$, yellow $[10^{-3} \leq \mathrm{Br}(h \to e\tau) < 1.5 \times 10^{-3}]$, green $[1.5 \times 10^{-3} \leq \mathrm{Br}(h \to e\tau) < 3.5 \times 10^{-3}]$, and red $[3.5 \times 10^{-3} \leq \mathrm{Br}(h \to e\tau) < 4.7 \times 10^{-3}]$.

whole and the dashed line part of 2×10^3 GeV$^2 < M^2_{\tilde{L}13} < 1.05 \times 10^5$ GeV^2 are in the gray area, and the dashed line of the rest exceeds the gray area. The contributions can obviously be influenced by the parameters $M^2_{\tilde{E}13}$ and $M^2_{\tilde{L}13}$.

Next, supposing the parameters with $M_S = 1.2$ TeV, we randomly scan the parameters. We scatter points for $h \to e\tau$ in Fig. 13. Some parameter ranges of $\tan\beta$, M_1, M_2, $M^2_{\tilde{L}ii}$, $M^2_{\tilde{E}ii}$, $M^2_{\tilde{\nu}ii}$, T_{eii}, and $T_{\nu ii}$ $(i = 1, 2, 3)$ are given in Table V. In addition, other parameter spaces are also represented in Table VI. We use blue $[0 < \mathrm{Br}(h \to e\tau) < 10^{-3}]$, yellow $[10^{-3} \leq \mathrm{Br}(h \to e\tau) < 1.5 \times 10^{-3}]$, green $[1.5 \times 10^{-3} \leq \mathrm{Br}(h \to e\tau) < 3.5 \times 10^{-3}]$, and red $[3.5 \times 10^{-3} \leq \mathrm{Br}(h \to e\tau) < 4.7 \times 10^{-3}]$ to represent the results in different parameter spaces for the process $h \to e\tau$.

Finally, we analyze the relationship between $M^2_{\tilde{L}13}$ and $M^2_{\tilde{E}13}$ in Fig. 13. All scatters are fan-shaped and evenly distributed, where four types of points are concentrated in 0 GeV$^2 < M^2_{\tilde{L}13} < 4.6 \times 10^5$ GeV^2. The blue parts are mainly in 0 GeV$^2 < M^2_{\tilde{L}13} < 2 \times 10^5$ GeV^2 and 0 GeV$^2 < M^2_{\tilde{E}13} < 1.3 \times 10^5$ GeV^2, yellow parts are mainly in 2×10^5 GeV$^2 < M^2_{\tilde{L}13} < 2.6 \times 10^5$ GeV^2 and 1.3×10^5 GeV$^2 < M^2_{\tilde{E}13} < 1.6 \times 10^5$ GeV^2, green parts are mainly in 2.6×10^5 GeV$^2 < M^2_{\tilde{L}13} < 4 \times 10^5$ GeV^2 and 1.6×10^5 GeV$^2 < M^2_{\tilde{E}13} < 2.5 \times 10^5$ GeV^2, and red parts are mainly in 4×10^5 GeV$^2 < M^2_{\tilde{L}13} < 4.6 \times 10^5$ GeV^2 and 2.5×10^5 GeV$^2 < M^2_{\tilde{E}13} < 2.9 \times 10^5$ GeV^2.

F. $h \to \mu\tau$

Finally, we analyze the process $h \to \mu\tau$ in the $U(1)_X$SSM. After experimental exploration, the experimental law of the $h \to \mu\tau$ process is similar to those of the $h \to e\mu$ and $h \to e\tau$ processes. When $M^2_{\tilde{E}23}$, $M^2_{\tilde{L}23}$, $T_{\nu 23}$ are variables, the corresponding branching ratios can reach 10^{-4}, 10^{-4}, 10^{-9}, respectively. It can be deduced that the parameters $M^2_{\tilde{E}23}$ and $M^2_{\tilde{L}23}$ are more sensitive than the parameter $T_{\nu 23}$.

Next, we scatter points on $h \to \mu\tau$ in Fig. 14 with the parameters in Table VII. These points are divided into blue $[0 < \mathrm{Br}(h \to \mu\tau) < 5 \times 10^{-4}]$, yellow $[5 \times 10^{-4} \leq \mathrm{Br}(h \to \mu\tau) < 1 \times 10^{-3}]$, green $[1 \times 10^{-3} \leq \mathrm{Br}(h \to \mu\tau) < 2 \times 10^{-3}]$, and red $[2 \times 10^{-3} \leq \mathrm{Br}(h \to \mu\tau) < 2.5 \times 10^{-3}]$ to represent the results in different parameter spaces for the process $h \to e\tau$.

We plot $M^2_{\tilde{E}23}$ varying with T_{e23} in Fig. 14(a), where we can see four of these points concentrated in 0 GeV$^2 < M^2_{\tilde{E}23} < 7 \times 10^4$ GeV^2. In Fig. 14(a), the blue parts are mainly in 0 GeV$^2 < M^2_{\tilde{E}23} < 3 \times 10^4$ GeV^2, yellow parts are mainly in 3×10^4 GeV$^2 < M^2_{\tilde{E}23} < 4.5 \times 10^4$ GeV^2, green parts are mainly in 4.5×10^4 GeV$^2 < M^2_{\tilde{E}23} < 6 \times 10^4$ GeV^2, and red parts are mainly in 6×10^4 GeV$^2 < M^2_{\tilde{E}23} < 7 \times 10^4$ GeV^2. In Fig. 14(b), we find that $T_{\nu 23}$ is not sensitive. The blue parts are mainly in 0 GeV$^2 < M^2_{\tilde{E}23} < 2.7 \times 10^4$ GeV^2, yellow parts are mainly in 2.7×10^4 GeV$^2 < M^2_{\tilde{E}23} < 4 \times 10^4$ GeV^2, green parts are mainly in 4×10^4

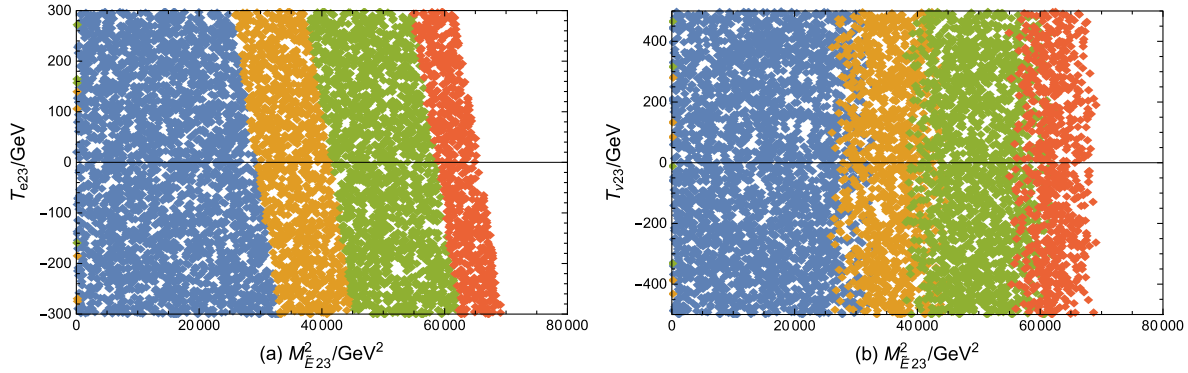

FIG. 14. Current limit on lepton flavor violating decay $h \to \mu\tau$. A reasonable parameter space is selected to scatter points, with blue $[0 < \mathrm{Br}(h \to \mu\tau) < 5 \times 10^{-4}]$, yellow $[5 \times 10^{-4} \leq \mathrm{Br}(h \to \mu\tau) < 1 \times 10^{-3}]$, green $[1 \times 10^{-3} \leq \mathrm{Br}(h \to \mu\tau) < 2 \times 10^{-3}]$, and red $[2 \times 10^{-3} \leq \mathrm{Br}(h \to \mu\tau) < 2.5 \times 10^{-3}]$.

$\mathrm{GeV}^2 < M^2_{\tilde{E}23} < 6 \times 10^4\ \mathrm{GeV}^2$, and red parts are mainly in $6 \times 10^4\ \mathrm{GeV}^2 < M^2_{\tilde{E}23} < 7 \times 10^4\ \mathrm{GeV}^2$. We can clearly see that the change trend of Fig. 14(a) is more obvious than that of Fig. 14(b).

VI. DISCUSSION AND CONCLUSION

In this paper, we study the LFV processes $Z \to l_i^{\pm} l_j^{\mp}$ and $h \to l_i^{\pm} l_j^{\mp}$ in the $U(1)_X$SSM. We take into account the one loop diagrams which include the self-energy diagram and the triangle diagram. In the numerical calculation, we scan large parameter spaces and find rich numerical results. In the parameter space we use, the numerical results show that the rates for $\mathrm{Br}(Z \to l_i^{\pm} l_j^{\mp})$ and $\mathrm{Br}(h \to l_i^{\pm} l_j^{\mp})$ can almost reach their present experimental upper bounds. The numerical analyses indicate that M_1, M_2, g_{YX}, $\tan\beta$ are important parameters. The sensitive parameters are $M^2_{\tilde{E}ij}$, $M^2_{\tilde{L}ij}$, $M^2_{\tilde{\nu}ij}$, $T_{\nu ij}$, and $T_{eij}(i \neq j)$ because they strongly affect the results. On the whole, the nondiagonal elements which correspond to the generations of the initial lepton and final lepton are the main sensitive parameters and LFV sources. Most parameters can break the upper limit of the experiment and provide new ideas for finding NP.

From the numerical results, the branching ratios of $Z \to e\mu$, $Z \to e\tau$, $Z \to \mu\tau$ and $h \to e\mu$, $h \to e\tau$, $h \to \mu\tau$ depend on the slepton flavor mixing parameters. Through data analysis, we find that the branching ratio of $Z \to e\mu$ can reach 10^{-11}. The branching ratios of $Z \to e\tau$ and $Z \to \mu\tau$ can reach 10^{-9}. The branching ratio of $h \to e\mu$ can reach 10^{-5}. The branching ratios of $h \to e\tau$ and $h \to \mu\tau$ can reach 10^{-3}. It is not difficult to find that the numerical results of the processes $h \to e\tau$ and $h \to \mu\tau$ are very close, and the numerical results of the processes $Z \to e\tau$ and $Z \to \mu\tau$ are very close. The branching ratios of $h \to e\mu$, $h \to e\tau$, $h \to \mu\tau$ in the $U(1)_X$SSM are close to the corresponding experimental upper limits of $\mathrm{Br}(h \to e\mu)$, $\mathrm{Br}(h \to e\tau)$, and $\mathrm{Br}(h \to \mu\tau)$, which may be detected in the future.

The numerical study is performed in terms of the most relevant model parameters. It shows that the flavor mixing parameters (such as $M^2_{\tilde{E}12}$ and $M^2_{\tilde{L}12}$) are very important and will be most efficiently tested at the LHC and future colliders (such as CEPC/FCC-ee). At future colliders, the higher statistics of Higgs boson and Z boson events will be achieved, and the sensitivities of future colliders can obviously be improved. Note that $M^2_{\tilde{E}12}$ and $M^2_{\tilde{L}12}$ are the core parameters for $Z \to e\mu$ and $h \to e\mu$. Larger $M^2_{\tilde{E}12}$ and $M^2_{\tilde{L}12}$ can obviously improve the branching ratios [$\mathrm{Br}(Z \to e\mu)$ and $\mathrm{Br}(h \to e\mu)$], and they are in the reachable region of the LHC. As the typical parameter of the $U(1)_X$SSM, M_S is the mass for the super partner of the Higgs singlet S, which appears in the mass squared matrix of the Higgs and the mass matrix of the neutralino. Thus, the search for M_S should relate to the Higgs decays, and the processes should relate to the neutralino. We hope that the LFV decays $Z \to l_i^{\pm} l_j^{\mp}$ and $h \to l_i^{\pm} l_j^{\mp}$ can be detected at the LHC and future colliders.

ACKNOWLEDGMENTS

This work is supported by the National Natural Science Foundation of China (NNSFC) (Grants No. 11535002 and No. 11705045), and the Natural Science Foundation of Hebei Province (Grant No. A2020201002).

APPENDIX: THE COUPLINGS

The concrete forms of the coupling coefficients corresponding to Fig. 1 are shown as follows:

Figure 1(a): $S_1 = \tilde{\nu}_n$, $S_2 = \tilde{\nu}_m$, $F = \chi^c$,

$$
\begin{aligned}
H_L^{S_2 F \bar{l}_i}(1) &= -\frac{1}{\sqrt{2}} U^*_{\alpha 2} Z^{I,*}_{mi} Y_{e,i}, \quad \left\langle \frac{i}{\sqrt{2}} U^*_{\alpha 2} Z^{R,*}_{mi} Y_{e,i} \right\rangle, \\
H_R^{S_2 F \bar{l}_i}(1) &= \frac{1}{\sqrt{2}} g_2 Z^{I,*}_{mi} V_{\alpha 1}, \quad \left\langle -\frac{i}{\sqrt{2}} g_2 Z^{R,*}_{mi} V_{\alpha 1} \right\rangle, \\
H_L^{S_1^* l_j \bar{F}}(1) &= -\frac{i}{\sqrt{2}} g_2 V^*_{\alpha 1} Z^{R,*}_{nj}, \quad \left\langle -\frac{1}{\sqrt{2}} g_2 V^*_{\alpha 1} Z^{I,*}_{nj} \right\rangle, \\
H_R^{S_1^* l_j \bar{F}}(1) &= \frac{i}{\sqrt{2}} U_{\alpha 2} Z^{R,*}_{nj} Y^*_{e,j}, \quad \left\langle \frac{1}{\sqrt{2}} U_{\alpha 2} Z^{I,*}_{nj} Y^*_{e,j} \right\rangle, \\
H^{Z S_1 S_2^*}(1) &= \frac{1}{\sqrt{2}} \Bigg((g_1 \cos\theta'_W \sin\theta_W + g_2 \cos\theta_W \cos\theta'_W - g_{YX} \sin\theta'_W) \sum_{a=1}^{3} Z^{I,*}_{m,a} Z^{R,*}_{n,a} \\
&\quad + (g_X \sin\theta'_W) \sum_{a=1}^{3} Z^{I,*}_{m,3+a} Z^{R,*}_{n,3+a} \Bigg) (-p_\mu^{\nu^R_{(n,m)}} + p_\mu^{\nu^I_{(m,n)}}).
\end{aligned} \tag{A1}
$$

Figure 1(b): $S_1 = \tilde{L}_n$, $S_2 = \tilde{L}_m$, $F = \chi^0$,

$$
\begin{aligned}
H_L^{S_2 F \bar{l}_i}(2) &= i\left(-\frac{1}{\sqrt{2}} 2 g_1 N_{\rho 1}^* Z_{m,3+i}^{E,*} - \frac{1}{\sqrt{2}}(2 g_{YX} + g_X) N_{\rho 5}^* Z_{m,3+i}^{E,*} - N_{\rho 3}^* Z_{m,i}^{E,*} Y_{e,i}\right), \\
H_R^{S_2 F \bar{l}_i}(2) &= i\left(\frac{1}{\sqrt{2}} Z_{m,i}^{E,*}(g_1 N_{\rho 1} + g_2 N_{\rho 2} + g_{YX} N_{\rho 5}) - Y_{e,i}^* Z_{m,3+i}^{E,*} N_{\rho 3}\right), \\
H_L^{S_1^* l_j \bar{F}}(2) &= i\left(\frac{1}{\sqrt{2}} g_1 N_{\rho 1}^* Z_{n,j}^{E} + \frac{1}{\sqrt{2}} g_2 N_{\rho 2}^* Z_{n,j}^{E} + \frac{1}{\sqrt{2}} g_{YX} N_{\rho 5}^* Z_{n,j}^{E} - N_{\rho 3}^* Y_{e,j} Z_{n,3+j}^{E}\right), \\
H_R^{S_1^* l_j \bar{F}}(2) &= i\left(-\frac{1}{\sqrt{2}} Z_{n,3+j}^{E}(2 g_1 N_{\rho 1} + (2 g_{YX} + g_X) N_{\rho 5}) - Y_{e,j}^* Z_{n,j}^{E} N_{\rho 3}\right), \\
H^{Z S_1 S_2^*}(2) &= \frac{i}{\sqrt{2}}\Bigg((-g_1 \cos\theta'_W \sin\theta_W + g_2 \cos\theta_W \cos\theta'_W + g_{YX} \sin\theta'_W) \sum_{a=1}^{3} Z_{n,a}^{E,*} Z_{m,a}^{E} \\
&\quad + (-2 g_1 \cos\theta'_W \sin\theta_W + 2 g_{YX} + 2 g_X) \sin\theta'_W \sum_{a=1}^{3} Z_{n,3+a}^{E,*} Z_{m,3+a}^{E}\Bigg).
\end{aligned} \tag{A2}
$$

Figure 1(c): $S_1 = H^{\pm}$, $S_2 = H^{\pm}$, $F = \nu$,

$$
\begin{aligned}
&H_L^{S_2 F \bar{l}_i}(3) = i U_{ki}^{V,*} Y_{e,i} Z_{m1}^{+}, \qquad H_R^{S_1^* l_j \bar{F}}(3) = i Y_{e,j}^* U_{kj}^{V} Z_{n1}^{+}, \\
&H_R^{S_2 F \bar{l}_i}(3) = H_L^{S_1^* l_j \bar{F}}(3) = 0, \\
&H^{Z S_1 S_2^*}(3) = \frac{i}{\sqrt{2}} \delta_{ij}(-g_1 \cos\theta'_W \sin\theta_W + g_2 \cos\theta_W \cos\theta'_W + (g_{YX} + g_X) \sin\theta'_W).
\end{aligned} \tag{A3}
$$

Figure 1(d): $F_1 = \chi_n^c$, $F_2 = \chi_m^c$, $S = \tilde{\nu}$,

$$
\begin{aligned}
H_L^{S F_2 \bar{l}_i}(4) &= -\frac{1}{\sqrt{2}} U_{m2}^* Z_{pi}^{I,*} Y_{e,i}, \quad \left\langle \frac{i}{\sqrt{2}} U_{m2}^* Z_{pi}^{R,*} Y_{e,i} \right\rangle, \\
H_R^{S F_2 \bar{l}_i}(4) &= \frac{1}{\sqrt{2}} g_2 Z_{pi}^{I,*} V_{m1}, \quad \left\langle -\frac{i}{\sqrt{2}} g_2 Z_{pi}^{R,*} V_{m1} \right\rangle, \\
H_L^{S^* l_j \bar{F}_1}(4) &= -\frac{1}{\sqrt{2}} g_2 Z_{pj}^{I,*} V_{n1}^*, \quad \left\langle -\frac{i}{\sqrt{2}} g_2 Z_{pj}^{R,*} V_{n1}^* \right\rangle, \\
H_R^{S^* l_j \bar{F}_1}(4) &= \frac{1}{\sqrt{2}} Z_{pj}^{I,*} Y_{e,j}^* U_{n2}, \quad \left\langle \frac{i}{\sqrt{2}} Z_{pj}^{R,*} Y_{e,j}^* U_{n2} \right\rangle, \\
H_L^{Z F_1 \bar{F}_2}(4) &= \frac{i}{\sqrt{2}}(2 g_2 U_{m1}^* \cos\theta_W \cos\theta'_W U_{n1} + U_{m2}^*(-g_1 \cos\theta'_W \sin\theta_W \\
&\quad + g_2 \cos\theta_W \cos\theta'_W + (g_{YX} + g_X) \sin\theta'_W) U_{n2}), \\
H_R^{Z F_1 \bar{F}_2}(4) &= \frac{i}{\sqrt{2}}(2 g_2 U_{n1}^* \cos\theta_W \cos\theta'_W U_{m1} + U_{n2}^*(-g_1 \cos\theta'_W \sin\theta_W \\
&\quad + g_2 \cos\theta_W \cos\theta'_W + (g_{YX} + g_X) \sin\theta'_W) U_{m2}).
\end{aligned} \tag{A4}
$$

Figure 1(e): $F_1 = \chi_n^0$, $F_2 = \chi_m^0$, $S = \tilde{L}$,

$$
\begin{aligned}
H_L^{SF_2\bar{l}_i}(5) &= i\left(-\frac{1}{\sqrt{2}} 2 g_1 N_{m1}^* Z_{k,3+i}^{E,*} - \frac{1}{\sqrt{2}}(2g_{YX} + g_X) N_{m5}^* Z_{k,3+i}^{E,*} - N_{m3}^* Z_{k,i}^{E,*} Y_{e,i}\right), \\
H_R^{SF_2\bar{l}_i}(5) &= i\left(\frac{1}{\sqrt{2}} Z_{k,i}^{E,*}(g_1 N_{m1} + g_2 N_{m2} + g_{YX} N_{m5}) - Y_{e,i}^* Z_{k,3+i}^{E,*} N_{m3}\right), \\
H_L^{S^* l_j \bar{F}_1}(5) &= i\left(\frac{1}{\sqrt{2}} g_1 N_{n1}^* Z_{k,j}^{E} + \frac{1}{\sqrt{2}} g_2 N_{n2}^* Z_{k,j}^{E} + \frac{1}{\sqrt{2}} g_{YX} N_{n5}^* Z_{k,j}^{E} - N_{n3}^* Y_{e,j} Z_{k,3+j}^{E}\right), \\
H_R^{S^* l_j \bar{F}_1}(5) &= i\left(-\frac{1}{\sqrt{2}} Z_{k,3+j}^{E}(2g_1 N_{n1} + (2g_{YX} + g_X) N_{n5}) - Y_{e,j}^* Z_{k,j}^{E} N_{n3}\right), \\
H_L^{ZF_1\bar{F}_2}(5) &= -\frac{i}{\sqrt{2}}(N_{m3}^*(g_1 \cos\theta_W' \sin\theta_W + g_2 \cos\theta_W \cos\theta_W' - (g_{YX} + g_X)\sin\theta_W') N_{n3} \\
&\quad \times N_{m4}^*(g_1 \cos\theta_W' \sin\theta_W + g_2 \cos\theta_W \cos\theta_W' - (g_{YX} + g_X)\sin\theta_W') N_{n4} \\
&\quad \times 2(-g_X \sin\theta_W'))(N_{m6}^* N_{n6} - N_{m7}^* N_{n7}))\gamma_\mu, \\
H_R^{ZF_1\bar{F}_2}(5) &= \frac{i}{\sqrt{2}}(N_{n3}^*(g_1 \cos\theta_W' \sin\theta_W + g_2 \cos\theta_W \cos\theta_W' - (g_{YX} + g_X)\sin\theta_W') N_{m3} \\
&\quad \times N_{n4}^*(g_1 \cos\theta_W' \sin\theta_W + g_2 \cos\theta_W \cos\theta_W' - (g_{YX} + g_X)\sin\theta_W') N_{m4} \\
&\quad \times 2(-g_X \sin\theta_W'))(N_{m6}^* N_{n6} - N_{m7}^* N_{n7}))\gamma_\mu.
\end{aligned} \tag{A5}
$$

Figure 1(f): $F_1 = \nu_n$, $F_2 = \nu_m$, $S = H^{\pm}$,

$$
\begin{aligned}
H_L^{SF_2\bar{l}_i}(6) &= i U_{mi}^{V,*} Y_{e,i} Z_{g1}^{+}, \qquad H_R^{S^* l_j \bar{F}_1}(6) = i Y_{e,j}^* U_{nj}^{V} Z_{g1}^{+}, \\
H_R^{SF_2\bar{l}_i}(6) &= H_L^{S^* l_j \bar{F}_1}(6) = 0, \\
H_L^{ZF_1\bar{F}_2}(6) &= -\frac{i}{\sqrt{2}}\left((g_1 \cos\theta_W' \sin\theta_W + g_2 \cos\theta_W \cos\theta_W' - g_{YX} \sin\theta_W') \sum_{a=1}^{3} U_{m,a}^{V,*} U_{n,a}^{V}\right. \\
&\quad \left. + (-g_X \sin\theta_W') \sum_{a=1}^{3} U_{m,3+a}^{V,*} U_{m,3+a}^{V}\right), \\
H_R^{ZF_1\bar{F}_2}(6) &= \frac{i}{\sqrt{2}}\left((g_1 \cos\theta_W' \sin\theta_W + g_2 \cos\theta_W \cos\theta_W' - g_{YX} \sin\theta_W') \sum_{a=1}^{3} U_{n,a}^{V,*} U_{m,a}^{V}\right. \\
&\quad \left. + (-g_X \sin\theta_W') \sum_{a=1}^{3} U_{n,3+a}^{V,*} U_{m,3+a}^{V}\right).
\end{aligned} \tag{A6}
$$

Figure 1(g): W_1, W_2, $F = \nu$,

$$
\begin{aligned}
H_L^{W_2 F \bar{l}_i}(7) &= -\frac{i}{\sqrt{2}} g_2 \sum_{a=1}^{3} U_{ka}^{V,*} \gamma_\mu, \qquad H_L^{W_1^* l_j \bar{F}}(7) = -\frac{i}{\sqrt{2}} g_2 \sum_{a=1}^{3} U_{ka}^{V} \gamma_\mu, \\
H_R^{W_2 F \bar{l}_i}(7) &= H_R^{W_1^* l_j \bar{F}}(7) = 0, \\
H^{ZW_1 W_2^*}(7) &= -i g_2 \cos\theta_W \cos\theta_W'(g_{\rho\mu}(-p_\sigma^{Z_\mu} + p_\sigma^{W_\rho^+}) + g_{\rho\sigma}(-p_\mu^{W_\rho^+} + p_\mu^{W_\sigma^-}) \\
&\quad + g_{\sigma\mu}(-p_\rho^{W_\sigma^-} + p_\rho^{Z_\mu})).
\end{aligned} \tag{A7}
$$

Figure 1(h): $F_1 = \nu_n$, $F_2 = \nu_m$, W,

$$
\begin{aligned}
H_L^{WF_2\bar{l}_i}(8) &= -\frac{i}{\sqrt{2}} g_2 \sum_{a=1}^{3} U_{ma}^{V,*}(\gamma_\mu P_L), \qquad H_L^{\bar{F}_1 l_j W^*}(8) = -\frac{i}{\sqrt{2}} g_2 \sum_{a=1}^{3} U_{na}^{V}(\gamma_\mu P_L), \\
H_R^{WF_2\bar{l}_i}(8) &= H_R^{\bar{F}_1 l_j W^*}(8) = 0, \\
H_L^{ZF_1\bar{F}_2}(8) &= -\frac{i}{\sqrt{2}} \Bigg((g_1 \cos\theta'_W \sin\theta_W + g_2 \cos\theta_W \cos\theta'_W - g_{YX} \sin\theta'_W) \sum_{a=1}^{3} U_{m,a}^{V,*} U_{n,a}^{V} \\
&\quad + (-g_X \sin\theta'_W) \sum_{a=1}^{3} U_{m,3+a}^{V,*} U_{m,3+a}^{V} \Bigg), \\
H_R^{ZF_1\bar{F}_2}(8) &= \frac{i}{\sqrt{2}} \Bigg((g_1 \cos\theta'_W \sin\theta_W + g_2 \cos\theta_W \cos\theta'_W - g_{YX} \sin\theta'_W) \sum_{a=1}^{3} U_{n,a}^{V,*} U_{m,a}^{V} \\
&\quad + (-g_X \sin\theta'_W) \sum_{a=1}^{3} U_{n,3+a}^{V,*} U_{m,3+a}^{V} \Bigg).
\end{aligned} \tag{A8}
$$

[1] Y. Abe *et al.* (Double-Chooz Collaboration), Phys. Rev. Lett. **108**, 131801 (2012).
[2] F. An *et al.* (Daya-Bay Collaboration), Phys. Rev. Lett. **108**, 171803 (2012).
[3] CMS Collaboration, Phys. Lett. B **716**, 30 (2012).
[4] CMS Collaboration, J. High Energy Phys. 06 (2013) 081.
[5] G. Aad *et al.* (ATLAS Collaboration), Phys. Rev. D **90**, 07 (2014).
[6] P. A. Zyla *et al.* (Particle Data Group), Prog. Theor. Exp. Phys. **2020**, 083C01 (2020).
[7] V. Cirigliano, K. Fuyuto, C. Lee, E. Mereghetti, and B. Yan, J. High Energy Phys. 03 (2021) 256.
[8] M. Dam, SciPost Phys. Proc. **01**, 041 (2019) [arXiv:1811.09408].
[9] G. Aad *et al.* (ATLAS Collaboration), Phys. Rev. Lett. **127**, 271801 (2022).
[10] L. Calibbi, X. Marcano, and J. Roy, Eur. Phys. J. C **81**, 12 (2021).
[11] A. M. Sirunyan *et al.* (CMS Collaboration), J. High Energy Phys. 06 (2018) 001.
[12] G. Aad *et al.* (ATLAS Collaboration), Phys. Lett. B **801**, 135148 (2020).
[13] G. Aad *et al.* (ATLAS Collaboration), Phys. Lett. B **800**, 135069 (2020).
[14] Q. Qin, Q. Li, C. D. Lü, F.-S. Yu, and S.-H. Zhou, Eur. Phys. J. C **78**, 835 (2018).
[15] Z. N. Zhang, H. B. Zhang, J. L. Yang, S.-M. Zhao, and T.-F. Feng, Phys. Rev. D **103**, 115015 (2021).
[16] D. W. Li, C. X. Yue, Y. Q. Wang *et al.*, Europhys. Lett. **137**, 03 (2022).
[17] O. Adriani *et al.* (L3 Collaboration), Phys. Lett. B **316**, 427 (1993).
[18] R. Akers *et al.* (OPAL Collaboration), Z. Phys. C **67**, 555 (1995).
[19] P. Abreu *et al.* (DELPHI Collaboration), Z. Phys. C **73**, 243 (1997).
[20] A. Brignole and A. Rossi, Phys. Lett. B **566**, 217 (2003).
[21] D. McKeen, M. Pospelov, and A. Ritz, Phys. Rev. D **86**, 113004 (2012).
[22] M. Arroyo, J. L. Diaz-Cruz, E. Diaz, and J. A. Orduz-Ducuara, Chin. Phys. C **40**, 123103 (2016).
[23] A. Falkowski, D. M. Straub, and A. Vicent, J. High Energy Phys. 05 (2014) 092.
[24] S. Baek, T. Nomura, and H. Okada, Phys. Lett. B **759**, 91 (2016).
[25] N. Bizot, S. Davidson, M. Frigerio, and J.-L. Kneur, J. High Energy Phys. 03 (2016) 073.
[26] C. Alvarado, R. M. Capdevilla, A. Delgado, and A. Martin, Phys. Rev. D **94**, 075010 (2016).
[27] B. Yang, J. Han, and N. Liu, Phys. Rev. D **95**, 035010 (2017).
[28] F. Staub, arXiv:0806.0538.
[29] F. Staub, Comput. Phys. Commun. **185**, 1773 (2014).
[30] F. Staub, Adv. High Energy Phys. **2015**, 840780 (2015).
[31] T. T. Wang, S. M. Zhao, X. X. Dong, L.-H. Su, Z.-N. Zhang, W. Li, and T.-F. Feng, J. High Energy Phys. 04 (2022) 122.
[32] B. Yan, S. M. Zhao, and T. F. Feng, Nucl. Phys. **B975**, 115671 (2022).
[33] S. M. Zhao, L. H. Su, X. X. Dong, T.-T. Wang, and T.-F. Feng, J. High Energy Phys. 03 (2022) 101.
[34] S. M. Zhao, T. F. Feng, M. J. Zhang, J.-L. Yang, H.-B. Zhang, and G.-Z. Ning, J. High Energy Phys. 02 (2020) 130.
[35] M. Carena, J. R. Espinosaos, and C. E. M. Wagner, Phys. Lett. B **355**, 209 (1995).
[36] M. Carena, S. Gori, N. R. Shah, and C. E. M. Wagner, J. High Energy Phys. 03 (2012) 014.
[37] G. Belanger, J. D. Silva, and H. M. Tran, Phys. Rev. D **95**, 115017 (2017).

[38] V. Barger, P. F. Perez, and S. Spinner, Phys. Rev. Lett. **102**, 181802 (2009).
[39] P. H. Chankowski, S. Pokorski, and J. Wagner, Eur. Phys. J. C **47**, 187 (2006).
[40] J. L. Yang, T. F. Feng, S. M. Zhao, R.-F. Zhu, X.-Y. Yang, and H.-B. Zhang, Eur. Phys. J. C **78**, 714 (2018).
[41] L. H. Su, S. M. Zhao, X. X. Dong, D.-D. Cui, T.-F. Feng, and H.-B. Zhang, Eur. Phys. J. C **81**, 433 (2021).
[42] S. M. Zhao, G. Z. Ning, J. J. Feng, H.-B. Zhang, T.-F. Feng, and X.-X. Dong, Nucl. Phys. **B969**, 115469 (2021).
[43] A. F. Tlalpaa, J. M. Hernandezb, G. T. Velascoa, and J. J. Toscano, Phys. Rev. D **65**, 073010 (2002).
[44] J. Hisano, T. Moroi, K. Tobe, and M. Yamaguchi, Phys. Rev. D **53**, 2442 (1996).
[45] H. B. Zhang, T. F. Feng, S. M. Zhao, and F. Sun, Int. J. Mod. Phys. A **29**, 1450123 (2014).
[46] S. Heinemeyer *et al.* (LHC Higgs Cross Section Working Group), Report No. CERN-2013-004 [arXiv:1307.1347].
[47] G. Aad *et al.* (ATLAS Collaboration), Phys. Lett. B **796**, 68 (2019).
[48] G. Cacciapaglia, C. Csaki, G. Marandella, and A. Strumia, Phys. Rev. D **74**, 033011 (2006).
[49] M. Carena, A. Daleo, B. A. Dobrescu, and T. M. P. Tait, Phys. Rev. D **70**, 093009 (2004).
[50] L. Basso, Adv. High Energy Phys. **2015**, 980687 (2015).
[51] P. Cox, C. C. Han, and T. T. Yanagida, Phys. Rev. D **104**, 075035 (2021).
[52] M. V. Beekveld, W. Beenakker, M. Schutten, and J. De Wit, SciPost Phys. **11**, 049 (2021).
[53] M. Chakraborti, L. Roszkowski, and S. Trojanowski, J. High Energy Phys. 05 (2021) 252.
[54] F. Wang, L. Wu, Y. Xiao, J. M. Yang, and Y. Zhang, Nucl. Phys. **B970**, 115486 (2021).
[55] M. Chakraborti, S. Heinemeyer, and I. Saha, Eur. Phys. J. C **81**, 1114 (2021).
[56] M. Endo, K. Hamaguchi, S. Iwamoto, and T. Kitahara, J. High Energy Phys. 07 (2021) 075.
[57] T. T. Wang, S. M. Zhao, J. F. Zhang *et al.*, Eur. Phys. J. C **82**, 7 (2022).